

AD-A110 947

MASSACHUSETTS INST OF TECH LEXINGTON LINCOLN LAB
SOLID STATE RESEARCH, 1981:2.(U)
MAY 81 A L MCWHORTER

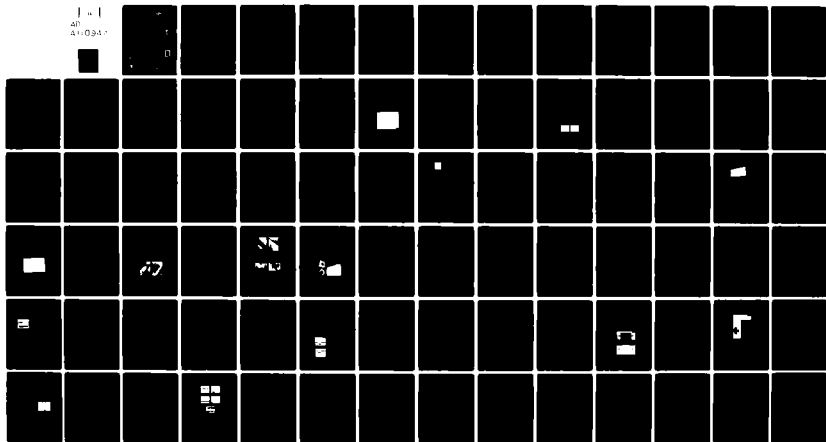
F/6 9/3

UNCLASSIFIED

ESD-TR-81-95

F19628-80-C-0002
NL

1 - 1
40
41-0947



END
DATE
FILMED
3-82
DTIC

LEVEL III

12

fu

A078676

AD A110947

2

DTIC ELECTED

FEB 16 1982

S

E

Solid State Research

1981

Prepared
under Electronic Systems Division Contract F19628-80-C-0002 by

Lincoln Laboratory

MASSACHUSETTS INSTITUTE OF TECHNOLOGY

LEXINGTON, MASSACHUSETTS



DTIC FILE COPY

Approved for public release; distribution unlimited.

82 02 16 006

The work reported in this document was performed at Lincoln Laboratory, a center for research operated by Massachusetts Institute of Technology, with the support of the Department of the Air Force under Contract ;F19628-80-C-0002.

This report may be reproduced to satisfy needs of U.S. Government agencies.

The views and conclusions contained in this document are those of the contractor and should not be interpreted as necessarily representing the official policies, either expressed or implied, of the United States Government.

The Public Affairs Office has reviewed this report, and it is releasable to the National Technical Information Service, where it will be available to the general public, including foreign nationals.

This technical report has been reviewed and is approved for publication.

FOR THE COMMANDER

Raymond J. Loiseau

Raymond L. Loiseau, Lt. Col., USAF
Chief, ESD Lincoln Laboratory Project Office

Non-Lincoln Recipients

PLEASE DO NOT RETURN

Permission is given to destroy this document
when it is no longer needed.

MASSACHUSETTS INSTITUTE OF TECHNOLOGY
LINCOLN LABORATORY

SOLID STATE RESEARCH

QUARTERLY TECHNICAL SUMMARY REPORT

1 FEBRUARY - 30 APRIL 1981

ISSUED 14 OCTOBER 1981

Approved for public release; distribution unlimited.

LEXINGTON

MASSACHUSETTS

ABSTRACT

This report covers in detail the solid state research work of the Solid State Division at Lincoln Laboratory for the period 1 February through 30 April 1984. The topics covered are Solid State Device Research, Quantum Electronics, Materials Research, Microelectronics, and Analog Device Technology. Funding is primarily provided by the Air Force, with additional support provided by the Army, DARPA, Navy, NASA, and DOE.

Accession For	
NTIS GRA&I	<input checked="" type="checkbox"/>
DTIC TAB	<input type="checkbox"/>
Unannounced	<input type="checkbox"/>
Justification	
Price	
Availability	
Avail. and/or	
Dist	Special
A	

DTIC
COPY
INSPECTED
2

PRECEDING PAGE BLANK-NOT FILMED

CONTENTS

Abstract	iii
Introduction	vii
Reports on Solid State Research	x
Organization	xviii
I. SOLID STATE DEVICE RESEARCH	1
A. Intracavity Loss Modulation of GaInAsP Diode Lasers	1
B. InP Optoelectronic Mixers	3
II. QUANTUM ELECTRONICS	9
A. Study of Feasibility of Laser Remote Sensing of Hydrazine, Monomethylhydrazine, and Unsymmetrical Dimethylhydrazine	9
1. Choice of Transition Lines for Differential-Absorption	9
2. Remote Sensing Detection Sensitivity of Hydrazine Compounds	9
3. Laboratory Absorption Measurements of Hydrazine Compounds	11
B. Spectral Linewidth Measurements of an External-Cavity Semiconductor Diode Laser	12
C. Nonlinear Spectroscopy of Semiconductors	18
III. MATERIALS RESEARCH	23
A. GaAs Shallow-Homojunction Solar Cells on Epitaxial Ge Grown on Si Substrates	23
B. Cathodoluminescence Analysis of Polycrystalline GaAs	27
C. Transient Annealing of Arsenic-Implanted Silicon Using a Graphite Strip Heater	32
D. Single-Crystal Si Films on SiO ₂ Prepared by Using a Stationary Graphite Heater for Lateral Epitaxy by Seeded Solidification	37
IV. MICROELECTRONICS	43
A. Charge-Coupled Devices: Imagers	43
B. Oxide Barriers to Formation of Refractory Silicides	47
C. Pattern Registration Using the Scanning Electron Beam Lithography System	50
V. ANALOG DEVICE TECHNOLOGY	55
A. Analog MNOS Memory: Speed and Endurance Capabilities and Correlator Performance	55
B. 2- to 20-GHz-Bandwidth Superconducting Matched Filter: Design Analysis	57
1. The Filter Concept	57
2. Analysis of Time-Bandwidth Constraints	61
3. Summary	67

INTRODUCTION

I. SOLID STATE DEVICE RESEARCH

GaInAsP/InP diode lasers have been fabricated with an intracavity electroabsorption modulator. The additional loss produced by operating the modulator near maximum reverse bias increased the laser threshold by a factor of as much as 2.9 relative to the threshold with the modulator open-circuited. Large depth of modulation of the laser output has been achieved at frequencies up to 2.5 GHz, the system measurement limit.

InP optoelectronic switches have been shown to have potential performance advantages over conventional diode bridges as electronic mixers. These advantages include isolation of local oscillator and signal, simplicity of construction, and linearity from low frequencies into the gigahertz range. Mixer operation has been demonstrated at 100 MHz, and calculations indicate good performance into the gigahertz range with existing InP technology and GaAs laser sources.

II. QUANTUM ELECTRONICS

A preliminary study, including laboratory measurements, has been made to test the capability of a dual-laser differential absorption LIDAR system for the remote sensing of hydrazine, monomethylhydrazine, and unsymmetrical dimethylhydrazine, which are used as aircraft and missile propellants. The results indicate that a detection sensitivity of 10 to 100 parts per billion in the atmosphere over a range of several kilometers should be achieved with these molecules.

Two GaAlAs double-heterostructure semiconductor diode lasers, each in a separate external cavity, have been heterodyned. Broadly tunable (10 nm), single longitudinal mode operation, with a spectral linewidth less than 15 kHz, has been observed for the first time.

The characteristic times for thermalization to the lattice temperature of electrons excited to the upper noncentral conduction-band minima of GaAs and InP have been measured using a four-wave mixing technique. Relaxation times of 1.1 ps for GaAs and 0.3 ps for InP at a lattice temperature of 300 K are obtained. Measurements of the nonresonant third-order susceptibility in these materials show that it is dominated by bound electron contributions and is insensitive to the free carrier concentration.

III. MATERIALS RESEARCH

Shallow-homojunction GaAs solar cells have been fabricated from single-crystal GaAs epilayers grown by chemical vapor deposition on Si substrates that were coated with a thin epilayer of vacuum-evaporated Ge to enhance GaAs nucleation. These cells, which have conversion efficiencies of 12 percent (AM1), are the first reported GaAs devices fabricated on Si substrates.

Cathodoluminescence excited by the electron beam of a scanning electron microscope has been utilized for nondestructive characterization of the optoelectronic properties of polycrystalline GaAs doped with Zn at the concentration level ($\sim 10^{19} \text{ cm}^{-3}$) used for the substrates of GaAs shallow-homojunction solar cells. By employing cathodoluminescence imaging and using spectral analysis to determine local carrier concentrations and diffusion lengths, it has been found that grain boundaries in this material differ significantly in their effects on nonradiative recombination and impurity distribution.

A simple transient annealing technique, which should be useful for large-scale semiconductor processing, has been developed for removal of ion-implantation damage in Si. For samples implanted with As at concentrations below the equilibrium solubility limit, annealing at 900° to 1000°C for only 10 seconds on a graphite strip heater results in electrical activation comparable to that obtained by a conventional furnace anneal at 1000°C for 30 min., but with negligible dopant redistribution.

A simplified version of the LESS technique (Lateral Epitaxy by Seeded Solidification) has been developed for the growth of single-crystal Si films over insulators. Films grown over SiO_2 by the new method, which uses a stationary graphite strip for transient heating, are comparable in crystal quality to the films obtained by the original method, which uses both a stationary heater and a movable heater.

IV. MICROELECTRONICS

The technique of charge skimming has been investigated for use with the CCD imager developed for the GEODSS (Ground-based Electro-Optical Deep Space Surveillance) Program as a means of increasing the sensitivity of the sensor for daylight sky surveillance, an application characterized by high background and low contrast. To demonstrate the capability of this technique, the final transfer stage of a CCD array has been operated with a signal of approximately 3,700 electrons electrically added to an optically induced background of 400,000 electrons.

A metallization technique, in which alternating films of silicon and a refractory metal are deposited from a multi-hearth electron-beam source without breaking vacuum, has been used to investigate the formation of refractory-metal silicides. Although TaSi_2 and MoSi_2 are readily formed by this technique, the chemistry of vacuum-deposited tungsten films results in an isolating oxide between the tungsten and silicon films that prevents the formation of WSi_2 up to 1000°C. This property of tungsten makes it inherently useful for buried-metal films in silicon devices.

The high-accuracy alignment capability of scanning electron-beam lithography systems has been applied to FET device patterns with submicrometer feature sizes. A multistep alignment procedure is used which involves coarse registration to large alignment marks viewed at low magnification, followed by high-resolution alignment using a set of small alignment marks imaged at high magnification.

V. ANALOG DEVICE TECHNOLOGY

Tests on MNOS/CCD analog memory chips indicate that the devices can withstand at least 10^6 erase/write cycles before the onset of degradation in writing and retention characteristics. Fixed-pattern noise is the major source of error in the memory and is caused by threshold voltage variations both in the thin-oxide (memory) dielectric (~ 40 mV) and in the thick-oxide (nonmemory) dielectric (~ 25 mV). The device also functions as a binary/analog memory correlator, with well over 40 dB of linear dynamic range demonstrated in the correlation of 15-bit M-sequences.

As part of an effort to utilize superconducting circuits to produce very wide-band analog-signal processors, a design analysis has been carried out for tapped-delay-line filters made with superconducting waveguiding structures. The constraints on delay and bandwidth set by conductor loss, dielectric loss, dispersion, crosstalk, and current technology have been determined for microstrip, stripline, and coplanar waveguides. Matched filters with time-bandwidth products of over 1000 and with bandwidths of 2 to 20 GHz appear feasible.

REPORTS ON SOLID STATE RESEARCH

15 February through 15 May 1981

PUBLISHED REPORTS

Journal Articles

<u>JA No.</u>			
5071	Phase Diagram for LPE Growth of GaInAsP Layers Lattice Matched to InP Substrates	J. J. Hsieh	IEEE J. Quantum Electron. <u>QE-17</u> , 118 (1981)
5140	Balloon-Borne Laser Heterodyne Radiometer for Measurements of Stratospheric Trace Species	R. T. Menzies* C. W. Rutledge* R. A. Zantesson* D. L. Spears	Appl. Opt. <u>20</u> , 536 (1981)
5144	Low Dark-Current, High Gain GaInAs/InP Avalanche Photodetectors	V. Diadiuk S. H. Groves C. E. Hurwitz G. W. Iseler	IEEE J. Quantum Electron. <u>QE-17</u> , 260 (1981)
5145	Laser-Induced Dielectric Breakdown in Cryogenic Liquids	S. R. J. Brueck H. Kildal	J. Appl. Phys. <u>52</u> , 1004 (1981)
5150	Gain Spectra in GaInAsP/InP Proton-Bombarded Stripe-Geometry DH Lasers	J. N. Walpole T. A. Lind J. J. Hsieh J. P. Donnelly	IEEE J. Quantum Electron. <u>QE-17</u> , 186 (1981)
5156	High-Resolution Double-Resonance Spectroscopy of $2\nu_3 + \nu_3$ Transitions in SF ₆	C. W. Patterson* R. S. McDowell* P. F. Moulton A. Mooradian	Opt. Lett. <u>6</u> , 93 (1981)
5159	Detection of the J = 6 → 5 Transition of Carbon Monoxide	P. F. Goldsmith* N. R. Erickson* H. R. Fetterman B. J. Clifton D. D. Peck P. E. Tannenwald G. A. Koepf** D. Buhl* N. McAvoy*	Astrophys. J. <u>243</u> , L79 (1981)
5160	Transmission Electron Microscopy and Ion-Channeling Studies of Heteroepitaxial Ge _{1-x} Si _x Films Produced by Transient Heating	B-Y. Tsauro J. C. C. Fan T. T. Sheng*	Appl. Phys. Lett. <u>38</u> , 447 (1981)

* Author not at Lincoln Laboratory.

JA No.

- | | | | |
|------|--|--|---|
| 5163 | Efficient Si Solar Cells by Laser Photochemical Doping | T. F. Deutsch
J. C. C. Fan
G. W. Turner
R. L. Chapman
D. J. Ehrlich
R. M. Osgood, Jr. | Appl. Phys. Lett. <u>38</u> , 144
(1981) |
| 5164 | Lateral Epitaxy by Seeded Solidification for Growth of Single-Crystal Si Films on Insulators | J. C. C. Fan
M. W. Geis
B-Y. Tsaur | Appl. Phys. Lett. <u>38</u> , 365
(1981) |
| 5170 | Solid-Phase Heteroepitaxy of Ge on <100> Si | B-Y. Tsaur
J. C. C. Fan
R. P. Gale | Appl. Phys. Lett. <u>38</u> , 176
(1981) |
| 5173 | Intracavity Loss Modulation of GaInAsP Diode Lasers | D. Z. Tsang
J. N. Walpole
S. H. Groves
J. J. Hsieh
J. P. Donnelly | Appl. Phys. Lett. <u>38</u> , 120
(1981) |
| 5177 | Laser Photochemical Microalloying for Etching of Aluminum Thin Films | D. J. Ehrlich
R. M. Osgood, Jr.
T. F. Deutsch | Appl. Phys. Lett. <u>38</u> , 399
(1981) |
| 5179 | Explosive Crystallization of Amorphous Germanium | H. J. Leamy*
W. L. Brown*
G. K. Celler*
G. Foti*
G. H. Gilmer*
J. C. C. Fan | Appl. Phys. Lett. <u>38</u> , 137
(1981) |
| 5191 | Fundamental Line Broadening of Single-Mode (GaAl)As Diode Lasers | M. W. Fleming
A. Mooradian | Appl. Phys. Lett. <u>38</u> , 511
(1981) |
| 5201 | Low-Loss GaAs Optical Waveguides Formed by Lateral Epitaxial Growth over Oxide | F. J. Leonberger
C. O. Bozler
R. W. McClelland
I. Melngailis | Appl. Phys. Lett. <u>38</u> , 313
(1981) |

Meeting Speeches

MS No.

- | | | | |
|-------|--|---|---|
| 4779D | Beam Annealing of Ion-Implanted GaAs and InP | J. C. C. Fan
R. L. Chapman
J. P. Donnelly
G. W. Turner
C. O. Bozler | Proc. MRS Annual Mtg. 1980:
<u>Laser and Electron-Beam
Solid Interactions and Ma-
terials Processing</u> (Elsevier
North-Holland, New York,
1981), pp. 261-274 |
|-------|--|---|---|

* Author not at Lincoln Laboratory.

<u>MS No.</u>			
5127B	Recent Advances in High Efficiency, Low-Cost GaAs Solar Cells	J. C. C. Fan C. O. Bozler R. P. Gale R. W. McClelland R. L. Chapman G. W. Turner H. J. Zeiger	Proc. IEEE Intl. Electron Devices Mtg., Washington, DC, 8-10 December 1980, pp. 534-537
5196	Electrode Band Structure and Interface States in Photoelectrochemical Cells	J. G. Mavroides J. C. C. Fan H. J. Zeiger	In <u>ACS Symposium Series</u> , No. 146, "Photoeffects at Semiconductor-Electrolyte Interfaces," A. J. Nozik, Ed. (American Chemical Society, New York, 1981), pp. 217-230
5394	Nonlinear Optics of Cryogenic Liquids	S. R. J. Brueck H. Kildal	<u>Proceedings of the Sergio Porto Memorial Conference</u> (Springer-Verlag, Heidelberg, 1981), p. 147
5427	Measurement of Phase Boundary Dynamics During Scanned Laser Crystallization of Amorphous Ge Films	R. L. Chapman J. C. C. Fan H. J. Zeiger R. P. Gale	Proc. MRS Annual Mtg. 1980: <u>Laser and Electron-Beam Solid Interactions and Materials Processing</u> (Elsevier North-Holland, New York, 1981), pp. 81-88
5433	Electromagnetic Long-Line Effects in Surface Wave Convolver	E. L. Adler*	<u>1980 Ultrasonics Symposium Proceedings</u> (IEEE, New York, 1980), pp. 82-87
5434	The Effect of Acoustic Dispersion and Attenuation on SAW Convolver Performance	E. L. Adler* J. H. Cafarella	<u>1980 Ultrasonics Symposium Proceedings</u> (IEEE, New York, 1980), pp. 1-4
5435	Attenuating Thin Films for SAW Devices	A. C. Anderson V. S. Dolat W. T. Brogan	<u>1980 Ultrasonics Symposium Proceedings</u> (IEEE, New York, 1980), pp. 442-445
5436	Self-Aligning Bilateral Chirp-Transform System	D. R. Arsenault V. S. Dolat	<u>1980 Ultrasonics Symposium Proceedings</u> (IEEE, New York, 1980), pp. 220-225
5437	LiNbO ₃ Surface-Acoustic-Wave Edge-Bonded Transducers on ST Quartz and <001>-Cut GaAs	D. E. Oates R. A. Becker	<u>1980 Ultrasonics Symposium Proceedings</u> (IEEE, New York, 1980), pp. 367-370
5438	Temperature-Stable RAC	D. E. Oates D. M. Boroson	<u>1980 Ultrasonics Symposium Proceedings</u> (IEEE, New York, 1980), pp. 272-276
5439	An Acoustoelectric Burst-Waveform Processor	S. A. Reible L. Yao	<u>1980 Ultrasonics Symposium Proceedings</u> (IEEE, New York, 1980), pp. 133-138

* Author not at Lincoln Laboratory.

<u>MS No.</u>			
5440	Nonlinearly Coupled Modes of Surface Acoustic Waves	N. P. Vlannes* A. Bers*	1980 Ultrasonics Symposium Proceedings (IEEE, New York, 1980), pp. 356-361
5441	High Performance Elastic Convolver with Parabolic Horns	I. Yao	1980 Ultrasonics Symposium Proceedings (IEEE, New York, 1980), pp. 37-42
5448	Hybrid Convolver/Binary Signal Processor Achieves High Processing Gain	R. P. Baker J. H. Cafarella	1980 Ultrasonics Symposium Proceedings (IEEE, New York, 1980), pp. 5-9
5462	Detectors for the 1.1-1.6 μ m Wavelength Region	C. E. Hurwitz	Proc. SPIE Vol. 239: <u>Guided-Wave Optical and Surface Acoustic Wave Devices, Systems and Applications</u> (Society of Photo-Optical Instrumentation Engineers, Bellingham, Washington, 1981), pp. 33-41
5479	State-of-the-Art in Coherent Near-mm Detectors	P. E. Tannenwald	Proc. SPIE Vol. 259: <u>Millimeter Optics</u> (Society of Photo-Optical Instrumentation Engineers, Bellingham, Washington, 1981), pp. 2-4
5489	A Closed-Form Analysis of Reflective-Array Gratings	P. V. Wright H. A. Haus*	1980 Ultrasonics Symposium Proceedings (IEEE, New York, 1980), pp. 282-287
5530	GaAs Monolithic Circuit for Millimeter-Wave Receiver Application	A. Chu W. E. Courtney L. J. Mahoney G. A. Lincoln W. Macropoulos R. W. Sudbury W. T. Lindley	1981 IEEE Intl. Solid-State Circuits Conf., Digest of Technical Papers, Vol. XXIV, New York, New York, 18-20 February 1981, pp. 144-145
5538	Lateral Epitaxy by Seeded Solidification for Growth of Single-Crystal Si Films on Insulators	J. C. C. Fan M. W. Geis B.-Y. Tsaur	Proc. 1980 IEEE Intl. Electron Devices Mtg., Washington, DC, 8-10 December 1980, p. 845
5567	Pulsed Plasma Source for X-Ray Lithography	S. M. Matthews* R. Stringfield* L. Roth* R. Cooper* N. P. Economou D. C. Flanders	Proc. SPIE Vol. 275: <u>Semiconductor Microlithography VI</u> (Society of Photo-Optical Instrumentation Engineers, Bellingham, Washington, 1981)
5596	Explosive Crystallization of Amorphous Ge Films	H. J. Leamy* W. L. Brown* G. K. Celler* G. Foti* G. H. Gilmer* J. C. C. Fan	Proc. MRS Annual Mtg. 1980: <u>Laser and Electron-Beam Solid Interactions and Materials Processing</u> (Elsevier North-Holland, New York, 1981), p. 89

* Author not at Lincoln Laboratory.

UNPUBLISHED REPORTS

Journal Articles

<u>JA No.</u>			
5166	Detectors for the 1.1-1.6 μm Wavelength Region	C. E. Hurwitz	Accepted by Opt. Eng.
5185	Heteroepitaxy of Vacuum-Evaporated Ge Films on Single-Crystal Si	B-Y. Tsaur M. W. Geis J. C. C. Fan R. P. Gale	Accepted by Appl. Phys. Lett.
5189	The Electro-Optic Application of InP	A. G. Foyt	Accepted by J. Cryst. Growth
5195	n^+ -InP Growth over InGaAs by Liquid Phase Epitaxy	S. H. Groves M. C. Plonko	Accepted by Appl. Phys. Lett.
5200	Hydroplane Polishing of Semiconductor Crystals	J. V. Gormley M. J. Manfra A. R. Calawa	Accepted by Rev. Sci. Instrum.
5215	Optical Properties of Proton Bombarded InP and GaInAsP	F. J. Leonberger J. N. Walpole J. P. Donnelly	Accepted by IEEE J. Quantum Electron.
5220	Spatially Delineated Growth of Metal Films via Photochemical Prenucleation	D. J. Ehrlich R. M. Osgood, Jr. T. F. Deutsch	Accepted by Appl. Phys. Lett.
5227	Transient Annealing of Arsenic-Implanted Silicon Using a Graphite Strip-Heater	B-Y. Tsaur J. P. Donnelly J. C. C. Fan M. W. Geis	Accepted by Appl. Phys. Lett.
5229	Effect of Turbulence Induced Correlation on DIAL Measurement Errors	D. K. Killinger N. Menyuk	Accepted by Appl. Phys. Lett.
5230	Temporal Correlation Measurements of Pulsed Dual CO ₂ LIDAR Returns	N. Menyuk D. K. Killinger	Accepted by Opt. Lett.
5242	MNOS/CCD Nonvolatile Analog Memory	R. S. Withers D. J. Silversmith R. W. Mountain	Accepted by IEEE Electron Dev. Lett.
5251	Sputtered Films for Wavelength-Selective Applications	J. C. C. Fan	Accepted by Thin Solid Films

Meeting Speeches*

<u>MS No.</u>			
4584E	New Developments and Applications of Submillimeter Heterodyne Detectors	H. R. Fetterman	Seminar, University of California, Los Angeles, 18 March 1981
5134A	Excimer Excitation of Lasers Via Bound-Free and Free-Bound Transitions	R. M. Osgood, Jr.	Seminar, University of Florida, Gainesville, 13 April 1981
5161B	The Permeable Base Transistor	C. O. Bozler	Seminar, Greater Boston IEEE Chapter, Lincoln Laboratory, 23 April 1981
5230A	Picosecond Optical Sampling	H. A. Haus [†] S. T. Kirsch [†] K. Mathyssek [†] F. J. Leonberger	} SPIE Los Angeles Technical Symp., North Hollywood, California, 9-13 February 1981
5619	High-Performance GaInAsP/InP Avalanche Photodetectors	V. Diadiuk S. H. Groves C. E. Hurwitz G. W. Iseler	
5620	Intracavity Loss Modulation of GaInAsP Lasers	D. Z. Tsang J. N. Walpole S. H. Groves J. J. Hsieh J. P. Donnelly	
5632	InP Optoelectronic Mixers	A. G. Foyt F. J. Leonberger R. C. Williamson	
5640	Guided-Wave Electrooptic Analog to Digital Converter	F. J. Leonberger	
5236G	Direct-Write Laser Processing for Microelectronics	R. M. Osgood, Jr. D. J. Ehrlich T. F. Deutsch	
5528A	Transferable Single-Crystal Films Using the CLEFT Process	C. O. Bozler	} Industrial Liaison Program Symp., M.I.T., 16 April 1981
5607A	Laser Photochemical Techniques	T. F. Deutsch	
5633	Novel Junction Formation Techniques	B-Y. Tsaur	

* Titles of Meeting Speeches are listed for information only. No copies are available for distribution.

† Author not at Lincoln Laboratory.

MS No.			
5638	Large-Grained or Single-Crystal Films on Amorphous Substrates	M. W. Geis	
5644	Tomorrow's Solar Cell Technology	J. C. C. Fan	Industrial Liaison Program Symp., M.I.T., 16 April 1981
5645	Gallium Arsenide Solar Cells: Material Growth	R. P. Gale	
5646	Gallium Arsenide Solar Cells: Cell Fabrication	G. W. Turner	
5548	Low Loss LiNbO ₃ Waveguide Bends with Coherent Coupling	J. M. Johnson F. J. Leonberger	
5552	An Integrated Optical Temperature Sensor	J. M. Johnson F. J. Leonberger G. W. Pratt, Jr.	Third International Conference on Integrated Optics, 1981, Fiber Optics Society, Washington, D.C., 1981
5568	Repetitive Q-Switching of Semiconductor Diode Lasers	D. Z. Liang J. N. Walpole	
5578	Progress in Long-Wavelength Sources and Detectors	C. E. Hurwitz	
5556A	Surface-Acoustic-Wave Signal-Processing Devices	R. W. Ralston	Surface Acoustic Wave Devices, 1981, IEEE Press, New York, 1981
5569	Interband Magneto-Optical Studies in In _{1-x} Ga _x As _y P _{1-y} Semiconducting Alloys	K. Alavi R. J. Aggarwal S. H. Groves	Applied Physics Letters, 38, 1981, American Physical Society, Washington, D.C., 1981
5573	Precision Collisional Line-shapes by Difference-Frequency Laser Spectroscopy	A. S. Pine	
5678	Liquid Phase Epitaxial Growth of Hg _{1-x} Cd _x Te from Te-Rich Solutions	T. C. Harman	SPLE Technical Conference on East '81, Washington, D.C., 20-24 April 1981
5696	Applications of InP Photoconductive Switches	F. J. Leonberger	
5597	The Role of the GaAs Substrate in Device Performance	R. A. Murphy	GaAs Workshop, Wakefield, Massachusetts, 11 March 1981
5607B	Pulsed UV Laser Doping of Semiconductors	T. F. Deutsch	Laser Workshop, M.I.T., 4-5 May 1981

* Author not at Lincoln Laboratory.

MS No.

5609 A	Divalent Transition-Metal Solid State Lasers	P. F. Moulton A. Mooradian	} Topical Mtg. on Tunable Laser Sources, Keystone, Colorado, 1-3 April 1981
5641	Frequency-Doubled Mini-TEA CO ₂ Laser System for Remote Sensing	N. Menyuk P. F. Moulton D. K. Killinger	
5620 A	Intracavity Loss Modulation of GaInAsP Lasers	D. Z. Tsang J. N. Walpole S. H. Groves J. J. Hsieh J. P. Donnelly	Optics and Quantum Elec- tronics Seminar, M.I.T., 18 March 1981

ORGANIZATION

SOLID STATE DIVISION

A. L. McWhorter, *Head*
I. Melngailis, *Associate Head*
J. F. Goodwin, *Assistant*
P. E. Tannenwald, *Senior Staff*

QUANTUM ELECTRONICS

A. Mooradian, *Leader*
P. L. Kelley, *Associate Leader*

Barch, W. E.	Fetterman, H. R.
Belanger, L. J.	Goodhue, W. D.*
Brueck, S. R. J.	Hancock, R. C.
Burke, J. W.	Killinger, D. K.
Bushee, J. F.	Menyuk, N.
Clahasy, C.*	Moulton, P. F.
Coulombe, M. J.	Osgood, R. M., Jr.
Danue, V.	Parker, C. D.
DeFeo, W. E.	Peck, D. D.
Deutsch, T. F.	Sullivan, D. J.
Ehrlich, D. J.	Welford, D.
Feldman, B.	

ELECTRONIC MATERIALS

A. J. Strauss, *Leader*
J. C. C. Fan, *Assistant Leader*
J. G. Mavroides, *Senior Staff*
H. J. Zeiger, *Senior Staff*

Anderson, C. H., Jr.	Krohn, L., Jr.
Button, M. J.	Mastromattei, E. L.
Chapman, R. L.	Nitishin, P. M.
Davis, F. M.	Owens, E. B.
Delaney, E. J.	Palm, B. J.
Fahey, R. E.	Pantano, J. V.
Finn, M. C.	Salerno, J. P.*
Foley, G. H.	Tracy, D. M.
Gale, R. P.	Tsaur, B-Y.
Iseler, G. W.	Turner, G. W.
Kolesar, D. F.	Vohl, P.

APPLIED PHYSICS

R. C. Williamson, *Leader*
C. E. Hurwitz, *Associate Leader*
T. C. Harman, *Senior Staff*
R. H. Kingston, *Senior Staff*
R. H. Rediker, *Senior Staff*

Amiento, C. A.*	Leonberger, F. J.
Calawa, A. R.	Liau, Z. L.
Carter, F. B.	Lind, T. A.
DeMeo, N. L., Jr.	McBride, W. F.
Diadiuk, V.	Orr, L.*
Donnelly, J. P.	Paladino, A. E.
Ferrante, G. A.	Plonko, M. C.
Foyt, A. G.	Schloss, R. P.*
Groves, S. H.	Spears, D. L.
Hovey, D. L.	Tsang, D. Z.
Lattes, A.*	Walpole, J. N.

ANALOG DEVICE TECHNOLOGY

E. Stern, *Leader*
J. H. Cafarella, *Assistant Leader*
R. W. Ralston, *Assistant Leader*

Anderson, A. C.	Leung, I.
Arsenault, D. R.	Lowrey, S. D.
Baker, R. P.	Lynch, J. T.
Becker, R. A.	Macedo, E. M., Jr.
Behrman, G. J.	Oates, D. E.
Brogan, W. T.	Reible, S. A.
Dolat, V. S.	Slattery, R. L.
Fischer, J. H.	Withers, R. S.
Flynn, G. T.	Wright, P. V.*
Holtham, J. H.	Yao, I.
Kernan, W. C.	

MICROELECTRONICS

W. T. Lindley, *Leader*
F. J. Bachner, *Associate Leader*
N. P. Economou, *Assistant Leader*
R. A. Murphy, *Assistant Leader*

Alley, G. D.	Felton, B. J.	Melngailis, J.†
Bozler, C. O.	Flanders, D. C.	Mountain, R. W.
Bromley, E. I.	Geis, M. W.	Nichols, K. B.
Burke, B. E.	Goeloe, G. T.*	Piacentini, W. J.
Cabral, S. M.	Gray, R. V.	Pichler, H. H.
Chiang, A. M.	Hansell, G. L.*	Rabe, S.
Chu, A.	Hawryluk, A. M.*	Rathman, D. D.
Clifton, B. J.	Lincoln, G. A., Jr.	Shaver, D. C.‡
Daniels, P. J.	Lysczarz, T. M.	Silversmith, D. J.
DeGraff, P. D.	Macropoulos, W.	Smythe, D. L., Jr.
Durant, G. L.	Mahoney, L. J.	Vigilante, J. L.
Efremow, N., Jr.	McClelland, R. W.	Vojak, B. A.
Eita, M. E.	McGonagle, W. H.	Wilde, R. E.

* Research Assistant

† Part Time

‡ Staff Associate

I. SOLID STATE DEVICE RESEARCH

A. INTRACAVITY LOSS MODULATION OF GaInAsP DIODE LASERS

Intracavity loss modulation of diode lasers is a possible alternative to conventional current modulation, particularly in applications requiring large depth of modulation at high rates where current modulation becomes increasingly difficult. Intracavity loss can be produced by integrating an electroabsorption modulator section with a waveguide section and an optical amplifier section as shown in Fig. 1-1.

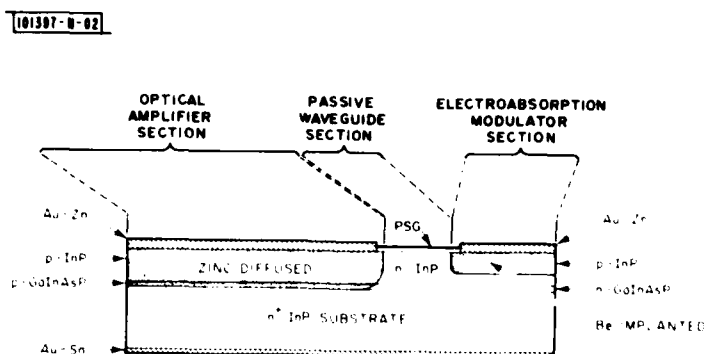


Fig. 1-1. Schematic drawing of the laser cross section. The optical amplifier and modulator range in length from 150 to 200 μm and 50 to 75 μm , respectively. The waveguide is 25 μm long. A mesa (not pictured) is etched to provide lateral optical confinement. The end-face mirrors are formed by cleaving.

The device structure has been fabricated from a conventional double-heterostructure wafer without the use of a tapered active region thickness or a varying material composition.¹ Optical gain is produced by the forward-biased double-heterostructure amplifier section. The electroabsorption loss takes place in the high-electric-field region of the reverse-biased p-n junction modulator section. The waveguide optically couples but electrically isolates the amplifier and the modulator. Complete isolation is ensured by making the waveguide longer than the sum of the modulator depletion width, the diffusion length of carriers injected from the amplifier section, and the width of any strain-enhanced lateral diffusion of zinc at the phosphosilicate glass-InP interface. The laser mirrors, shown at each end of the structure in Fig. 1-1, are formed by cleaving.

The device structure was grown by liquid-phase epitaxy (LPE) on a (100)-oriented InP(Sn) substrate doped to $2 \times 10^{18} \text{ cm}^{-3}$. The step-cooling technique was used to grow a 0.2- μm -thick active layer of $\text{Ga}_{0.23}\text{In}_{0.77}\text{As}_{0.52}\text{P}_{0.48}$ and a 2- μm -thick InP cap layer. The net donor concentration in both layers was $\sim 1 \times 10^{16} \text{ cm}^{-3}$. An InP buffer layer was not needed because an atmosphere of PH_3 in H_2 was used to prevent thermal etching of the substrate prior to growth.

Zinc was diffused through a window 10 to 12 μm wide in a phosphosilicate glass (PSG) mask to form a p-n junction for the amplifier section. A modulator section approximately 25 μm wide and 50 μm long was formed by selective implantation of Be ions into the InP cap, followed by annealing at 700 $^\circ\text{C}$ for 10 min. with a PSG cap layer in a flowing atmosphere of PH_3 and N_2 (Ref. 2). The InP and GaInAsP epitaxial layers were masked and etched to leave a mesa 25 μm

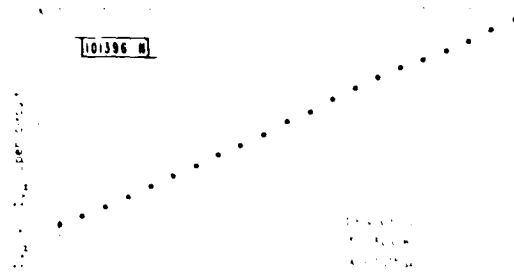


Fig. 1-2. Pulsed threshold, normalized to the threshold of the laser with the modulator open-circuited, as a function of the modulator reverse bias.



Fig. 1-3. Detected waveform of the laser output with a 2.2-GHz modulation signal applied to the modulator. The horizontal scale is 2 ns per major division.

wide for lateral optical confinement in the waveguide and modulator sections. Plated Au-Zn contacts were microalloyed to the Zn-diffused and Be-implanted regions through a PSG insulator mask layer, and plated Au-Sn contacts were microalloyed to the n^+ substrate. Ti and Au were sputtered and photolithographically defined to form contact pads on the p side.

Pulsed laser threshold currents of 260 to 300 mA with the modulator open-circuited were typical. Figure 1-2 shows the threshold of one device, relative to the threshold with the modulator open-circuited, plotted as a function of the DC modulator reverse bias. The pulsed threshold increased by a factor of about 2.9 upon application of a 20-V reverse bias, just below the modulator breakdown voltage of 22 V.

The lasers have been Q-switched at repetition frequencies between 1.7 and 2.5 GHz by application of a CW microwave signal to the modulator and an electrical pulse to the amplifier. The operating point of the modulator can be determined with a DC bias, which is generally set at a voltage near half breakdown. The electrical pulse to the optical amplifier is then increased until the laser turns on, and the microwave voltage swing is adjusted between the forward-conduction and reverse-breakdown voltages of the modulator. Typically, the microwave drive is about 200 mW into the unmatched circuit. A GaInAsP/InP photodiode with <100 ps rise and fall times is used to detect the laser emission.

The detector output, as displayed on a Tektronix 7104 oscilloscope with 1-GHz bandwidth, is shown in Fig. 1-3 for a modulation frequency of 2.2 GHz. It can be seen that the laser responds at this frequency after initial transients have decayed. The apparent depth of modulation is limited to about 50 percent by the oscilloscope frequency response, which is down approximately 15 dB at 2.2 GHz. Large-signal modulation has been observed between 1.7 and 2.5 GHz. Above 2.5 GHz, the oscilloscope was not capable of providing useful data.

Additional high-frequency measurements, utilizing a sampling oscilloscope, provided a better indication of the depth of modulation. Since the optical-amplifier pulse and the microwave signal are not synchronized, the nonrepetitive nature of the signal precludes a true representation of the waveform. Nevertheless, the observation that the sample points fill in between the baseline of the trace and the highest points indicates that the depth of modulation is substantially greater than the 50 percent seen in Fig. 1-3 and that the laser is likely turning on and off at frequencies as high as 2.5 GHz, the limit of the present measurements.

Further work will be necessary to define the capabilities and limitations of this modulation technique.

D. Z. Tsang J. J. Hsieh
J. N. Walpole J. P. Donnelly
S. H. Groves

B. InP OPTOELECTRONIC MIXERS

InP optoelectronic switches³ are undergoing development for use as electronic mixers. These devices offer several potential performance advantages over conventional diode mixers, including such important features as isolation of local oscillator and signal, simplicity of construction, and linearity from low frequencies into the gigahertz range.

As discussed by Clarke and Hess,⁴ switches may be used as mixers. Figure 1-4 illustrates one possible configuration. As shown, the switch $s(t)$ modulates the input $v_1(t)$ to give the output $v_2(t)$. Clearly, when $s(t)$ is closed, $v_1(t) = v_2(t)$, and when $s(t)$ is open, $v_2(t) = 0$. In other words, $v_1(t)$ is multiplied by, with, or mixed with $s(t)$. This multiplying function, which is also known as chopper modulation, may be described analytically as shown. If we are interested in the term

106214-N-02

CHOPPER MODULATION

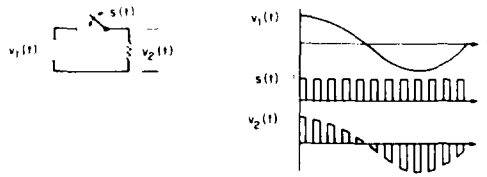
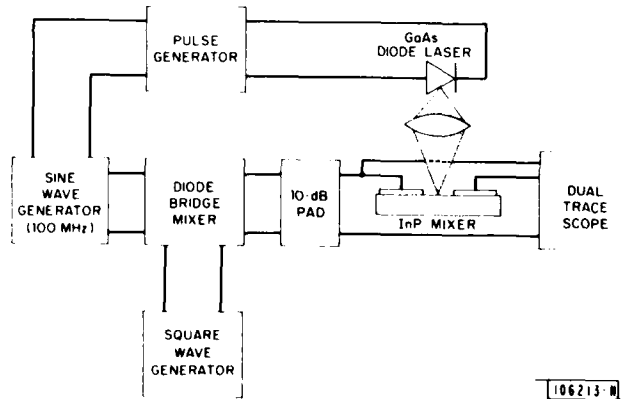


Fig. 1-4. Illustration of the use of a switch as a mixer. The three parts of the figure show the simplified mixer circuit, the voltage and switch waveforms, and the algebraic expansion of the mixer output.

$$v_2(t) = v_1(t) \cdot s(t)$$

$$= \frac{v_1(t)}{2} + \frac{2}{\pi} v_1(t) \cos \omega_0 t - \frac{3}{2\pi} v_1(t) \cos 3\omega_0 t + \dots$$



106213-N

Fig. 1-5. Schematic drawing of the demodulation experiment used to demonstrate mixer operation of an InP optoelectronic switch. The device used in this test was of the gap-structure type with a 3- μm gap.

involving the fundamental of the switch period and the input signal, filtering can be used to minimize the other terms. This process becomes more difficult, however, as the bandwidths of $s(t)$ and/or $v_1(t)$ are increased and the unwanted terms become included in the passband of the output filter. Another technique for suppressing unwanted terms in mixer response is to employ a device which is bilinear, i.e., the output is linear in both the RF and LO drive signals. When the LO applied to such a mixer is sinusoidal, instead of chopped as $s(t)$ is in Fig. I-4, one eliminates the higher order terms.

As shown above, switches can be used effectively as mixers. The InP optoelectronic switch has a number of important advantages relative to conventional mixers. These devices provide essentially total isolation between the local-oscillator and the other mixer ports, thus eliminating any leakage of the local-oscillator signal to the output IF port. There are no nonlinear elements such as diodes which generate and mix harmonics of both RF and LO signals, thus introducing spurious signals that limit the usable bandwidth of conventional mixers. The fact that there is no DC offset in the mixer output simplifies the design and operation of circuits in which the mixer output is video, i.e., low-pass filtered. Because the optoelectronic mixer is linear in both RF signal and light intensity, the device has potential for operation in a bilinear mode with the previously discussed advantages. In addition, the mixers are simple to fabricate.

On the other hand, optoelectronic mixers have a number of disadvantages. These devices require a modulated source of intense light, typically a laser. This requirement suggests that these mixers will need higher local-oscillator power than diode bridges, because lasers are at best only moderately efficient. Also, as the required modulation speeds begin to exceed 1 GHz, the demands on the laser source become substantial and, in fact, approach the limits of modulation speed for diode lasers. Furthermore, the on-state impedance of current devices is of the order of 100 Ω , thus producing several dB of mixer conversion loss in a 50- Ω circuit. However, this situation is expected to improve considerably as a result of further device development, and can be dramatically improved by going to impedance-matched configurations.

A demodulation experiment, shown schematically in Fig. I-5, was done to demonstrate mixer operation of the InP switch. In this experiment, a 100-MHz sine wave was modulated with square waves of different periods in a conventional diode-bridge mixer, and the resulting signal fed to the input of the InP device. The device was illuminated with light from a GaAs diode laser whose output intensity was synchronized with the sine wave, and the resulting mixer output was observed on a dual-trace oscilloscope, along with the input to the InP mixer. The results for two different square-wave periods are shown in Fig. I-6, where the device output is seen to be a faithful reproduction of the envelope of the input, as expected.



Fig. I-6. Results of the demodulation experiments of Fig. I-5 at two different square-wave periods. The harmonic content evident in the input signals is introduced by the diode-bridge modulator.

The discussion up to this point has centered on the development and evaluation of InP mixers with low on-state impedances for efficient mixer operation in broadband systems. If one employs impedance matching to better match the on-state mixer resistance to the impedance of a 50- Ω circuit, it is possible to obtain efficient mixer operation even at relatively low light levels as long as ω is small in comparison to the cutoff frequency ω_c . Impedance matching usually imposes a reduction in the fractional RF bandwidth over which the mixer is useful. However, in many applications, this bandwidth narrowing would be of relatively little consequence.

TABLE I-1 PROJECTED PERFORMANCE OF IMPEDANCE-MATCHED InP OPTOELECTRONIC MIXERS				
Photoconductive Lifetime (ps)	1000	50	10	1
Maximum Operating Frequency (GHz)	0.16	3.2	16	160
Minimum Feature Size l (μm)	2	1	0.5	0.25
Capacitance (fF)	5	10	20	40
On-State Resistance (ohms) for $\omega = 0.1 \omega_c$	20×10^3	500	50	2.5
Required Laser Power (mW)	0.0015	0.3	3.75	188
Device area = $20 \times 20 \mu\text{m}^2$				
Electron mobility = $4000 \text{ cm}^2/\text{V-s}$				

Performance anticipated for optoelectronic mixers over a wide range of frequencies is summarized in Table I-1. A primary parameter is the photoconductive lifetime in InP. The first two columns cover the range of photoconductive lifetimes that have been observed to date, and the final two columns indicate what could be achieved if the lifetime could be further reduced. For each case, the maximum frequency is inversely proportional to the lifetime. The minimum feature sizes shown are representative of current state of the art in the first two columns and of straightforward development in the last two columns. For good switch and mixer performance, it is desirable that the device on-state resistance be less than one-tenth of the off-state impedance, or equivalently $\omega_c > 10 \omega$. This criterion establishes the maximum on-state

resistances and thus the minimum required laser powers. It is assumed that impedance matching can be employed to match the mixer to the surrounding circuitry. The power levels in the first three columns are well within the state of the art of current diode lasers.

A. G. Foyt
F. J. Leonberger
R. C. Williamson

REFERENCES

1. F. K. Reinhart and R. A. Logan, *Appl. Phys. Lett.* 25, 622 (1974).
2. J. P. Donnelly and C. A. Armiento, *Appl. Phys. Lett.* 34, 96 (1979), DDC AD-A069910/8.
3. F. J. Leonberger and P. F. Moulton, "High Speed InP Optoelectronic Switch," *Appl. Phys. Lett.* 35, 712 (1979), DDC AD-A085785/4.
4. Kenneth K. Clarke and Donald T. Hess, Communication Circuits: Analysis and Design (Addison-Wesley, Reading, Massachusetts, 1978).

II. QUANTUM ELECTRONICS

A. STUDY OF FEASIBILITY OF LASER REMOTE SENSING OF HYDRAZINE, MONOMETHYLHYDRAZINE, AND UNSYMMETRICAL DIMETHYLHYDRAZINE

The suitability of the dual-CO₂ laser differential-absorption LIDAR (DIAL) system¹ for the remote sensing of hydrazine, unsymmetrical dimethylhydrazine (UDMH), and monomethylhydrazine (MMH) is being investigated; hydrazine, UDMH, and MMH are used as aircraft and missile propellants. The initial phase of this effort involved (a) the determination of the appropriate CO₂ laser transitions for the remote sensing of the hydrazine compounds, (b) theoretical estimates of the expected detection sensitivity as a function of range for remote sensing measurements with the system, and (c) laboratory measurements and verification of the differential-absorption coefficients of the compounds.

1. Choice of Transition Lines for Differential-Absorption

The choice of CO₂ laser frequencies to be used for remote sensing of the hydrazines included consideration of (a) those CO₂ frequencies obtainable with the mini-TEA CO₂ lasers,² (b) the differential-absorption of the hydrazine compounds at these frequencies, as taken from the measurements of Loper *et al.*,³ and (c) the atmospheric transmission⁴ and interference from other atmospheric species such as ammonia and ethylene^{5,6} at the chosen frequencies.

By using the above criteria, CO₂ laser frequencies were chosen to yield as large a differential absorption as possible consistent with minimal interference effects from either ammonia or ethylene. While it is desirable to choose the frequency pairs close together in order to maximize the mutual coherence of the two laser beams, this proved difficult to achieve for both UDMH and MMH. The explicit frequency choices along with the pertinent absorption parameters are given in Table II-1.

2. Remote Sensing Detection Sensitivity of Hydrazine Compounds

In general, one of two possible approaches is usually taken to determine the minimum concentration, n_{\min} , of a trace species as a function of range, R . The first establishes the limitation by setting the difference in the backscattered return at the two frequencies equal to the noise signal. The second approach assumes a limitation in the ability to distinguish changes below some predetermined value in the difference between the return signals (ΔP_p) at the two frequencies. The effects of both limitations have been considered for each of the hydrazines. The basis for the calculations have been given previously⁷ and will not be repeated here.

For the case in which the difference in return signals is set equal to the noise signal, it may be shown that n_{\min} , expressed directly in parts per billion, is given by

$$n_{\min} \text{ (ppb)} = \frac{5R}{\Delta\sigma \exp(-2\beta R)} \quad (\text{II-1})$$

where R is the range in km, $\Delta\sigma$ is the difference in the molecular absorption coefficients of the trace species at the two LIDAR wavelengths in units of $(\text{cm-atm})^{-1}$ and β is the atmospheric extinction coefficient in km^{-1} . In deriving Eq. (II-1) use was made of parameter values appropriate to the DIAL system, including a noise signal of 7×10^{-8} W, a receiver area of 600 cm^2 , and a peak pulse power of 10^5 W; a 10-percent system efficiency and a 10-percent topographic target reflectivity were assumed.

TABLE II-1
RELEVANT ABSORPTION PARAMETERS
FOR THE REMOTE SENSING OF THE HYDRAZINES

CO ₂ Laser Transition	Wavelength (μm)	Absorption Coefficients (cm-atm) ⁻¹				Atmospheric* Attenuation β(km) ⁻¹
		Hydrazine		NH ₃ †	C ₂ H ₄ †	
		(a)	(b)			
P(22)	10.611	5.27	5.41	0.045	1.09	0.1142
P(28)	10.675	2.26	2.17	0.36	1.30	0.0976
Differential Absorption		3.01	3.24	-0.315	-0.21	
		UDMH		NH ₃	C ₂ H ₄	
P(30)	10.696	2.28	1.45	0.86	1.63	0.0907
R(10)	10.318	0.11	0.05	0.78	1.51	0.1142
Differential Absorption		2.17	1.40	0.06	0.12	
		MMH		NH ₃	C ₂ H ₄	
R(30)	10.182	1.32	1.36	0.029	0.56	0.1137
R(18)	9.282	0.29	0.23	0.13	0.61	0.1418
Differential Absorption		1.03	1.13	-0.10	-0.05	

(a) This work
(b) Reference 3
* Reference 4
† Reference 5

Under high signal-to-noise conditions, such as occur at relatively short ranges, a more valid approach is to establish the minimum relative difference in the two differential-absorption LIDAR returns ($\Delta P_r/P_r$) that can be measured. Assuming that value to be 1 percent leads to a minimum detectable concentration⁷ of

$$n_{\min} (\text{ppb}) = \frac{50}{\Delta\sigma R} \quad (II-2)$$

With the use of Eqs. (II-1) and (-2) and the appropriate values of $\Delta\sigma$ and β , as given in Table II-1, the minimum detectable concentrations of the hydrazine-related molecules have been determined as a function of range for a single pulse pair. The results are given in Fig. II-1, which indicate that remote sensing of these molecules in concentrations of the order of 10 to 100 ppb is feasible at ranges up to 5 km. These results are subject to further improvement by averaging over several pulses.

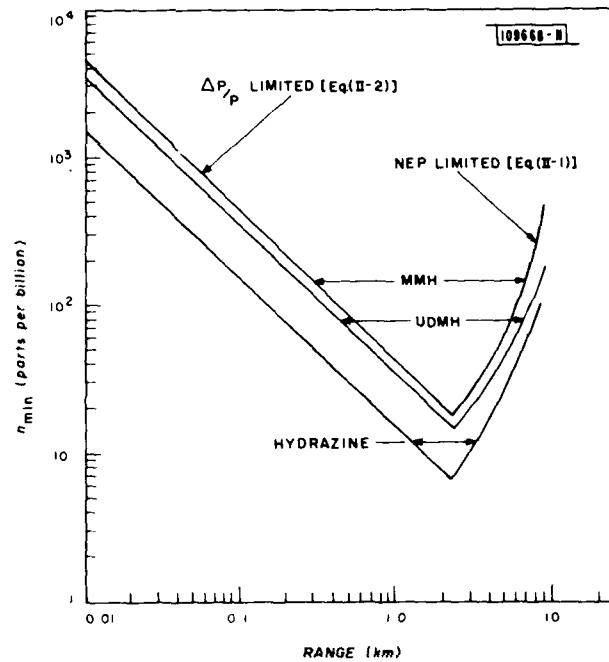


Fig. II-1. Minimum detectable average concentrations of hydrazine, unsymmetrical dimethylhydrazine (UDMH), and monomethylhydrazine (MMH) by topographic reflection as a function of range using a single 10-mJ, 100-ns laser pulse.

3. Laboratory Absorption Measurements of Hydrazine Compounds

Absorption measurements of the hydrazines for the chosen frequency pairs were carried out in the laboratory using the dual-laser DIAL system. The measurements involved firing the first laser at the on-resonance CO_2 laser frequency followed 50 μs later by the second laser firing at the off-resonance frequency. After passage through a beam splitter, both laser beams followed identical paths through an absorption cell containing either air or nitrogen at atmospheric

pressure. After establishing the 100-percent transmittance level of the normalized laser beams by averaging over 1000 pulses, a known volume of a hydrazine-related compound in liquid form was inserted into the cell and the laser beam transmittance measured as a function of time. Initial values of the relative transmittance were taken for every 100 pulses; after the rate of change declined, values were taken of the average of 500 pulses from each laser.

The measurements in a nitrogen atmosphere were made to determine if the calculated results given above, which were based on measurements by Loper *et al.* using a low-pressure CW CO₂ laser, are applicable to absorption measurements taken with a pulsed CO₂ TEA laser operating at atmospheric pressure. The results are shown in Figs. II-2, II-4, and II-6, and the absorption coefficients obtained from these measurements are given in Table II-1. The values for hydrazine and MMH agree with those obtained by Loper *et al.*,³ but the present values are 50 percent higher for UDMH.

The hydrazines are known to be strongly subject to oxidation effects,^{8,9} therefore, measurements in air cannot be used to measure absorption coefficients. However, since such measurements more closely simulate the effect of remote sensing of these molecules in the open atmosphere, they served to establish the feasibility of accurately following the changing concentration and to uncover additional problems which will be encountered in attempting to determine hydrazine concentrations in the atmosphere. The optical transmittance through the air-filled absorption cell as a function of time after insertion of the hydrazine compounds is given in Figs. II-3, II-5, and II-7.

Experiments are planned which involve placing a large cell containing known amounts of hydrazine compounds between the laboratory and topographic targets at 2.5 km in order to establish the ability to monitor the presence of these compounds over distances of several kilometers. Calculations, supported by the results discussed here, indicate that the detection of 10- to 100-ppb concentrations over ranges of a few kilometers is feasible.

N. Menyuk
D. K. Killinger

B. SPECTRAL LINEWIDTH MEASUREMENTS OF AN EXTERNAL-CAVITY SEMICONDUCTOR DIODE LASER

Recently the operation of an external-cavity semiconductor injection laser has been shown¹⁰ to be a stable, tunable, single-frequency source suitable for spectroscopic applications beyond the capabilities attainable using a monolithic semiconductor laser.¹¹ The external-cavity diode laser is composed of an AR-coated double-heterostructure GaAlAs laser diode positioned between a pair of AR-coated lenses which collect and collimate the diode radiation onto a first-order Littrow-configuration diffraction grating reflector at one end of the cavity and onto a partially reflecting dielectric mirror at the other end of the cavity. The laser cavity oscillates in a single longitudinal mode tunable over a 10-nm spectral range with output powers up to 5 mW. Measurements of the mode spectral width using a high-resolution scanning Fabry-Perot interferometer show an instrument-limited spectral linewidth of 3.5 MHz with a frequency jitter of 500 kHz rms.

Extrapolation of the typical spectral linewidth from a monolithic diode laser leads to estimates of a few hundred hertz (at the output powers available) for the linewidth of the external-cavity laser. In order to accurately determine the spectral linewidth, two external-cavity diode lasers were tuned to within 1 GHz with the aid of a high-resolution spectrometer and a scanning

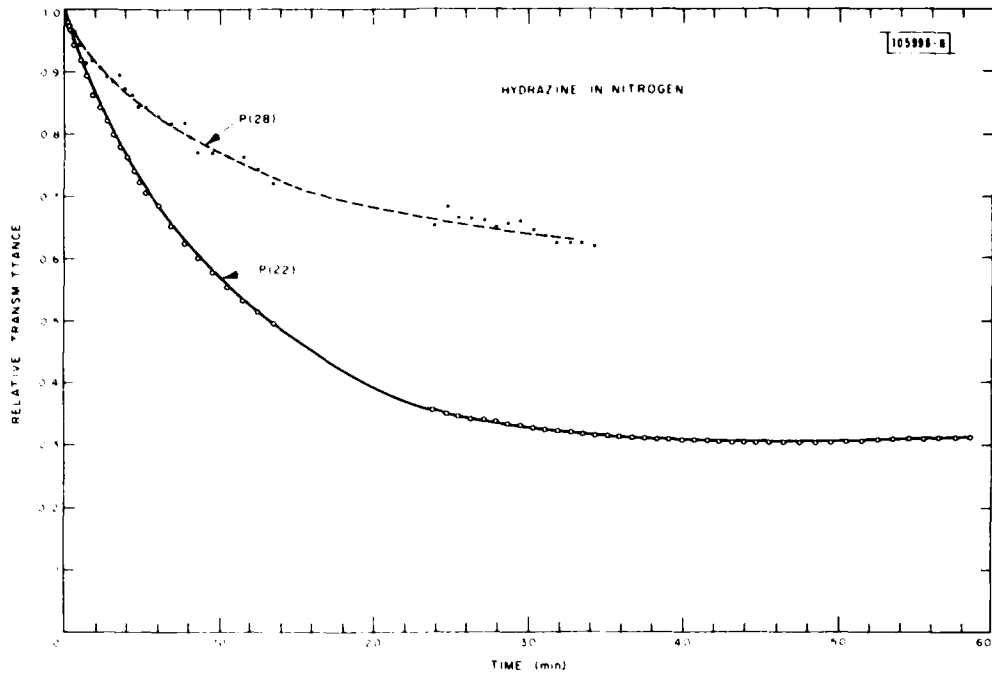


Fig. II-2. Time variation of relative transmittance of 10.6- μm P(22) and 10.7- μm P(28) radiation through absorption cell containing nitrogen after inserting 1.6 μl of liquid hydrazine.

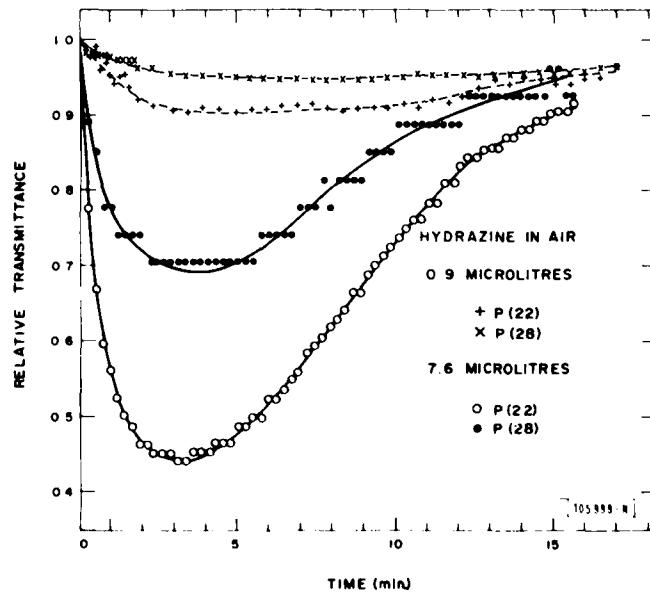


Fig. II-3. Time variation of relative transmittance of 10.6- μm P(22) and 10.7- μm P(28) radiation through absorption cell containing air after insertion of 0.9 and 7.6 μl of liquid hydrazine.

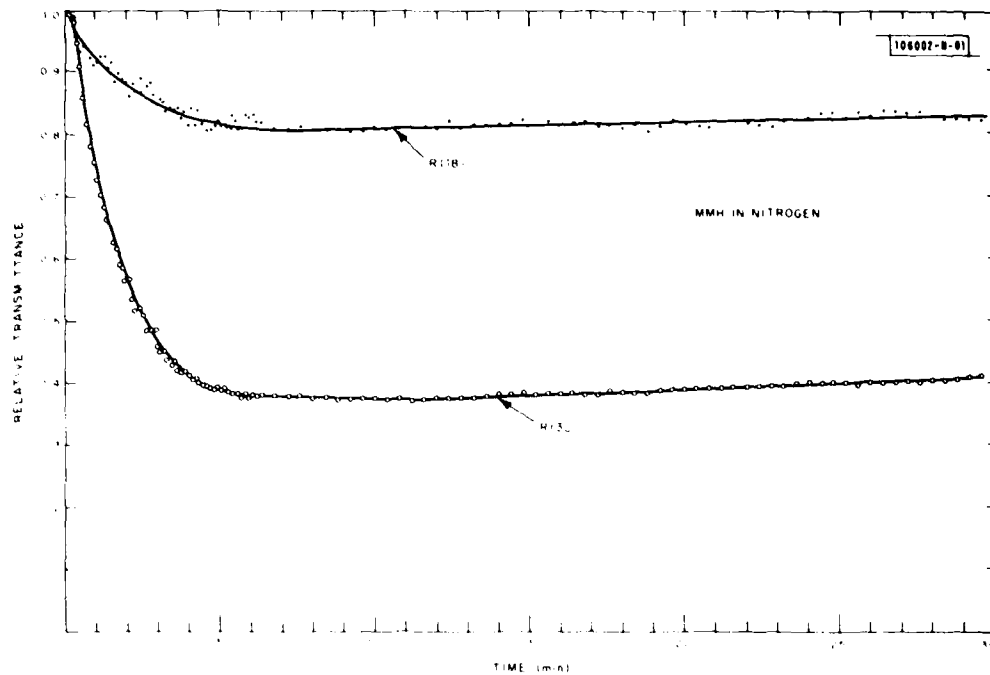


Fig. II-4. Time variation of relative transmission of 10.2- μm R(30) and 9.3- μm R(18) radiation through absorption cell containing nitrogen after inserting 0.3 μl of liquid MMH.

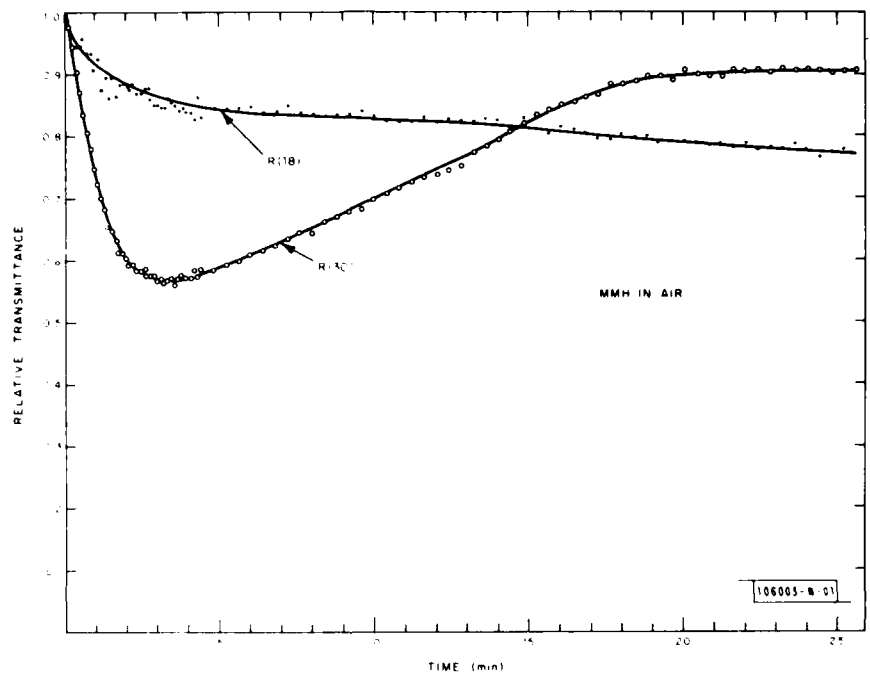


Fig. II-5. Time variation of relative transmission of 10.2- μm R(30) and 9.3- μm R(18) radiation through absorption cell containing air after inserting $9 \mu\text{l}$ of liquid MMH.

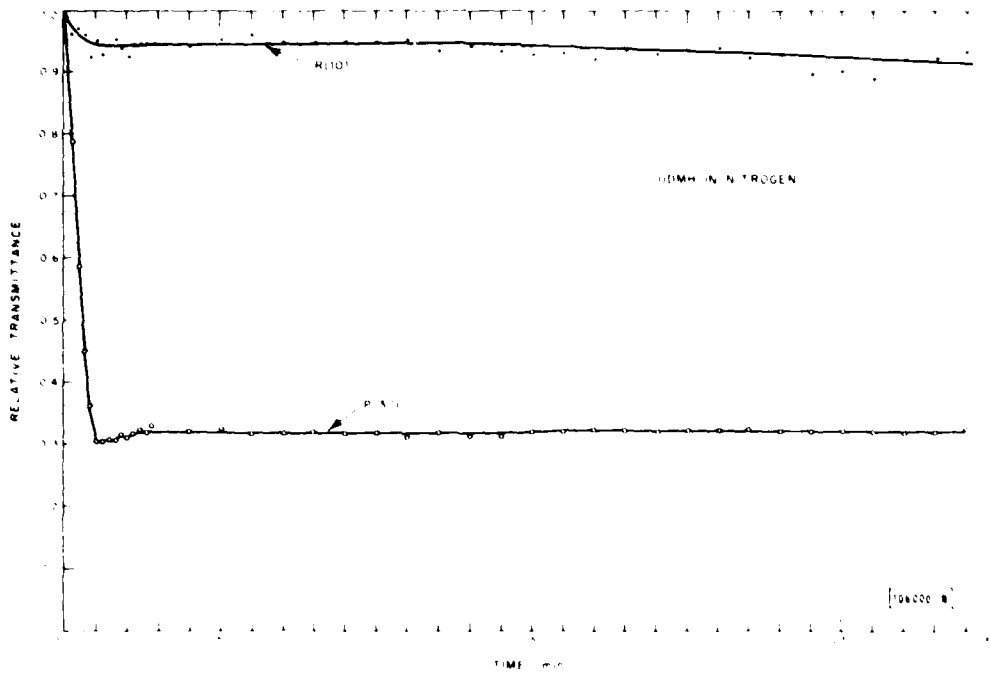


Fig. II-6. Time variation of relative transmission of 10.7- μm P(30) and 10.3- μm R(10) radiation through absorption cell containing nitrogen after inserting 9 μl of liquid UDMH.

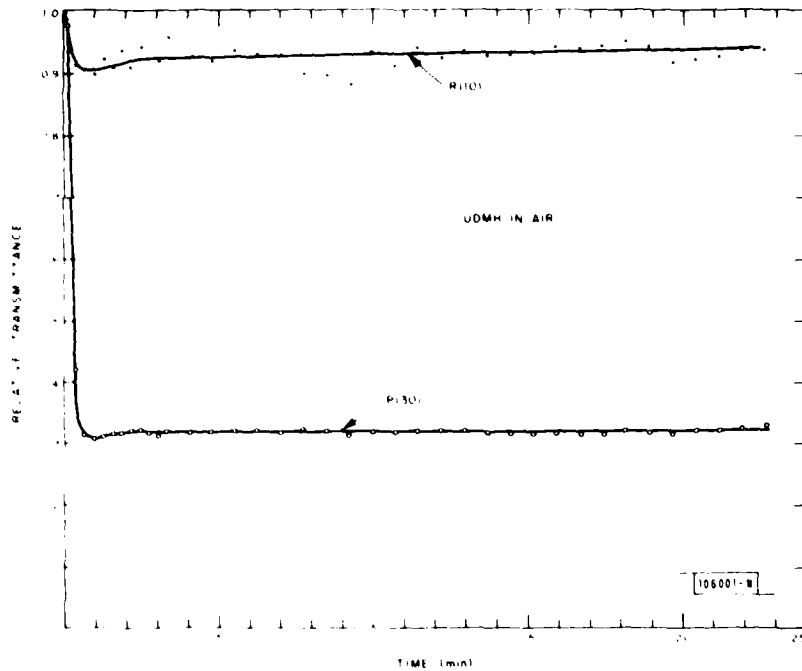


Fig. II-7. Time variation of relative transmission of 10.7- μm P(30) and 10.3- μm R(10) radiation through absorption cell containing air after inserting 9 μl of liquid UDMH.

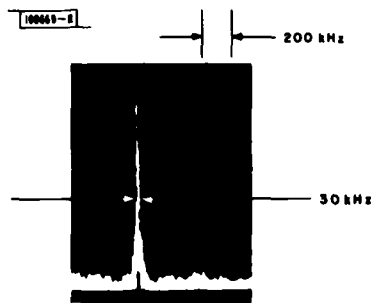


Fig. II-8. A heterodyne beat spectrum of two external-cavity diode lasers with 0.4- and 0.34-mW output powers.

Fabry-Perot interferometer. A heterodyne beat spectrum of the lasers could then be taken by mixing their outputs on a fast avalanche photodiode. Figure II-8 shows an instrument-limited heterodyne spectrum of 30-kHz width, implying a single-laser spectral linewidth of less than 15 kHz (Lorentzian lineshape). Higher resolution measurements were precluded because of frequency jitter of the individual lasers during the spectrum analyzer scan.

This is the first demonstration that an external-cavity GaAlAs semiconductor diode laser is capable of operation with a spectral linewidth less than 15 kHz. This result is approximately an order of magnitude greater than the theoretical estimate of the laser linewidth and is due to acoustic coupling of the surrounding environment to the cavity and presumably could be reduced by acoustical isolation.

D. Welford
A. Mooradian

C. NONLINEAR SPECTROSCOPY OF SEMICONDUCTORS

Previously, initial results were reported¹² of an investigation of the use of nonlinear spectroscopic techniques for semiconductor material diagnostics. Measurements using these techniques to probe hot-electron dynamics in III-V semiconductors and to study the nonresonant third-order nonlinear susceptibilities of III-V semiconductors have been made. The measurements were carried out using four-wave mixing techniques in which two input laser beams at frequencies ω_1 and ω_2 are spatially and temporally overlapped in the sample. Nonlinear mixing in the sample results in the generation of sidebands at $2\omega_1 - \omega_2$ and $2\omega_2 - \omega_1$ which are monitored as a function of the frequency difference $\omega_1 - \omega_2$. The experimental arrangement has been described in more detail previously. Briefly, two laser beams at wavelengths near 1 μm (in the transparency range of GaAs and InP) are generated by a flash-lamp-pumped Q-switched 1.06- μm YAG laser and by Raman shifting the output of a rhodamine 590 dye laser pumped by the second harmonic of the YAG laser in a high-pressure H_2 cell. The second Stokes output of the Raman cell is tunable from $+530 \text{ cm}^{-1}$ to -400 cm^{-1} around the 1.06- μm YAG output by tuning the dye laser.

The dynamics of hot-electron relaxation in GaAs and InP are crucial to the operation of high-frequency transferred-electron (TE) semiconductor devices such as Gunn oscillators.¹³ These devices depend upon the variation of an electron's mass and mobility between the central valley at the bottom of the conduction band and higher minima along the L and X crystallographic directions. High-frequency operation of these devices is limited by the relaxation of

hot electrons from these upper valleys back to the lattice temperature in the central minimum. Notwithstanding the importance of the relaxation process to the operation of TE devices, only very limited experimental information has been reported¹⁴ because of a lack of suitable experimental techniques.

The four-wave mixing experiment reported here gives a direct measure of this relaxation time. Phonon-assisted optical transitions between the Γ and X minima have been observed in both GaAs (Ref. 15) and InP (Ref. 16). Hot electrons are expected¹³ to relax quickly to the lowest noncentral valley (L minimum); relaxation from this valley back to the bottom of the Γ minimum is the rate-limiting step in the overall relaxation process. Because of the large difference in the electron masses between the bottom of the Γ minimum and the upper sections of the conduction band, an electron makes very different contributions to the medium polarizability depending upon its position within the band. This mechanism has previously been shown¹⁷ to lead to a contribution to the third-order nonlinear susceptibility $\chi^{(3)}$. This previous calculation was for a degenerate case where all frequencies were the same; extending the result to the case of two-frequency excitation gives

$$\chi^{(3)}(2\omega_1 - \omega_2, \omega_1, \omega_1, -\omega_2) = \chi_{\text{bound}}^{(3)} + \frac{\sigma e^2 c N T}{6\pi\hbar\omega_1^3} \left(\frac{R_{\Gamma}}{m_{\Gamma}} - \frac{R_L}{m_L} \right) \frac{1}{1 + i(\omega_1 - \omega_2)T} \quad (\text{II-3})$$

where $\chi_{\text{bound}}^{(3)}$ is the background nonlinearity of the bound electrons, σ is the absorption cross section, N the electron density, T the hot-electron relaxation time, and m_{Γ} and m_L the respective electron masses. R_{Γ} and R_L are resonance enhancement factors given by

$$R_j = \frac{1}{\epsilon_j^2 - (\hbar\omega_j)^2} \quad (j = \Gamma, L) \quad (\text{II-4})$$

where ϵ_j is the appropriate electronic energy above the valence band. These resonance factors also lead to a decrease in the electronic polarizability in the upper valleys as compared with the central valley. Measurements of the frequency response of the four-wave mixing signal ($\chi^{(3)}(\omega_1, \omega_1, \omega_1, -\omega_2)$) can thus be used to evaluate the relaxation time T . The results of this measurement are shown for a $1 \times 10^{18} \text{ cm}^{-3}$ n-type GaAs sample in Fig. II-9 and for a $3.7 \times 10^{18} \text{ cm}^{-3}$ n-type InP sample in Fig. II-10. For low concentration samples, the $\chi^{(3)}$ contribution due to the electron intervalley processes is masked by the background susceptibility, and no spectral structure was observed. For the two spectra, the solid curves are least-squares fits of Eq.(II-3) to the data and give an energy relaxation time of $T = 9 \times 10^{-13} \text{ s}$ for GaAs and $T = 3 \times 10^{-13} \text{ s}$ for InP. The more rapid hot-electron cooling in InP is expected¹³ because of the higher LO phonon energy and greater ionicity in this material. The relative values are consistent with the observed cutoff frequencies of TE devices in these two materials.

Limited measurements of the temperature dependences of these relaxation times have been carried out. At a lattice temperature of 430 K, the GaAs relaxation time has decreased to $\sim 8 \times 10^{-13} \text{ s}$. More extensive measurements over a broader temperature range are presently under way.

An understanding of the background $\chi^{(3)}$ contribution to the four-wave mixing process is clearly important. If this contribution could be reduced by a judicious choice of experimental parameters, it would allow measurement of the relaxation times over a wider parameter range.

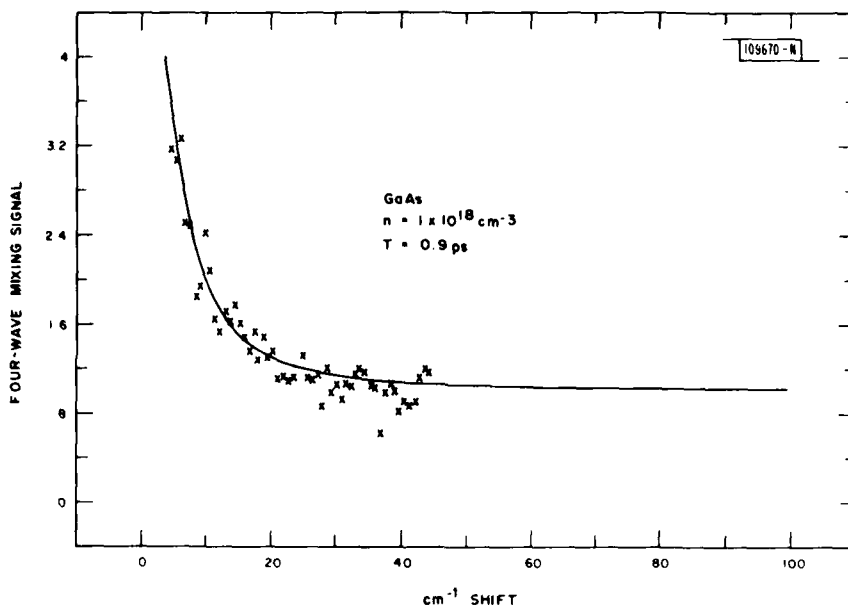


Fig. II-9. Variation in the four-wave mixing signal at $2\omega_1 - \omega_2$ as the frequency difference $\omega_1 - \omega_2$ is varied for a $n = 1 \times 10^{18} \text{ cm}^{-3}$ GaAs sample. The solid curve is a least-squares fit to the data and gives the relaxation time $0.9 \times 10^{-12} \text{ s}$.

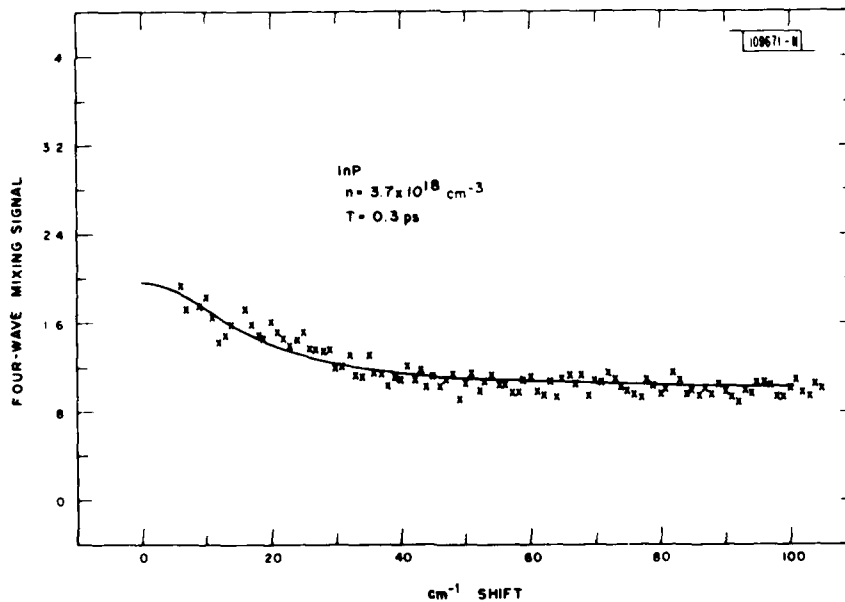


Fig. II-10. Variation in the four-wave mixing signal at $2\omega_1 - \omega_2$ as the frequency difference $\omega_1 - \omega_2$ is varied for a $n = 3.7 \times 10^{18} \text{ cm}^{-3}$ InP sample. The solid curve is a least-squares fit to the data and gives the relaxation time $0.3 \times 10^{-12} \text{ s}$.

In addition, in a recent publication, Kupecek *et al.*¹⁸ have reported CARS spectra of the LO phonon in GaAs similar to those in our previous report.¹² In their analysis they assumed a background $\chi^{(3)}$ proportional to the free-carrier concentration and used the interference between the background and phonon contributions to $\chi^{(3)}$ to obtain a measurement of the carrier concentration. We have measured the off-resonance (at $\omega_1 - \omega_2 \sim 100 \text{ cm}^{-1}$) background susceptibility in a wide range of GaAs materials ranging from semi-insulating Cr-doped to heavily doped ($\sim 10^{18} \text{ cm}^{-3}$) n- and p-type wafers. The variation in the background susceptibility was less than 20 percent over this entire parameter range. Thus, the reported interference technique does not provide a suitably sensitive technique for monitoring electron concentrations. Measurements and analysis are currently under way to provide a more complete understanding of the background susceptibility contributions as they are important for all types of nonlinear optical measurements.

S. R. J. Brueck

REFERENCES

1. N. Menyuk and D. K. Killinger, *Opt. Lett.*, **1**, 304 (1981).
2. N. Menyuk and P. F. Moulton, *Rev. Sci. Instrum.*, **51**, 216 (1980), DTIC AD-A085766-1.
3. G. I. Loper, A. R. Calloway, M. A. Stamps, and J. A. Gelbwachs, *Appl. Opt.*, **19**, 2726 (1980).
4. R. A. McClatchey, R. W. Fenn, J. E. A. Selby, F. E. Volz, and J. S. Garing, "Optical Properties of the Atmosphere (Third Edition)," Report AFGL-72-047, Environmental Research Paper No. 411 (1972).
5. R. R. Patty, G. M. Russwurm, W. A. McClenny, and D. R. Morgan, *Appl. Opt.*, **13**, 2850 (1974).
6. A. Mayer, G. Comera, H. Charpentier, and C. Jaussaud, *Appl. Opt.*, **17**, 34 (1978); and **19**, 1572 (1980).
7. A. Mooradian, D. K. Killinger, and N. Menyuk, "Remote Sensing of Turbine Engine Gases," Final Report, Lincoln Laboratory, M.I.T. (30 September 1979), ESD-TR-79-11; ESI-TR-80-09, DDC AD-A084544-6.
8. D. A. Stone, "The Autoxidation of Hydrazine and Unsymmetrical Dimethylhydrazine," Paper No. 13 in Proceedings of the Conference on Environmental Chemistry of Hydrazine Fuels, CEEDO-TR-78-14 (1978).
9. D. A. Stone, "The Autoxidation of Monomethylhydrazine Vapor," Report No. ESI-TR-79-10 (1979).
10. M. W. Fleming and A. Mooradian, *IEEE J. Quantum Electron.*, **QE-17**, 44 (1981).
11. M. W. Fleming and A. Mooradian, *Appl. Phys. Lett.*, **38**, 511 (1981).
12. Solid State Research, Lincoln Laboratory, M.I.T. (1980:4), p. 11, DTIC AD-A099742.
13. B. K. Ridley, *J. Appl. Phys.*, **48**, 754 (1977).
14. C. V. Shank, R. L. Fork, R. F. Leheney, and J. Shah, *Phys. Rev. Lett.*, **42**, 112 (1979).
15. I. Balslev, *Phys. Rev.*, **173**, 762 (1968).
16. W. P. Dumke, M. R. Lorenz, and G. D. Pettit, *Phys. Rev. B*, **1**, 4668 (1970).
17. Solid State Research, Lincoln Laboratory, M.I.T. (1980:3), p. 14, DTIC AD-A094075.
18. P. L. Kupecek, M. Comte, and D. S. Chemla, *Appl. Phys. Lett.*, **38**, 44 (1981).

III. MATERIALS RESEARCH

A. GaAs SHALLOW-HOMOJUNCTION SOLAR CELLS ON EPITAXIAL Ge GROWN ON Si SUBSTRATES

We have previously reported¹⁻⁴ the fabrication of single-crystal GaAs shallow-homojunction solar cells that have conversion efficiencies exceeding 20% (AM1). These cells employ an n⁺/p/p⁺ structure prepared by chemical vapor deposition (CVD) on either GaAs or Ge substrates. This report describes the fabrication of GaAs shallow-homojunction solar cells, with conversion efficiencies of 12% (AM1), prepared from GaAs epilayers grown on Ge/Si single-crystal substrates. These are the first reported GaAs devices fabricated on Si substrates.

Our primary motivation for investigating Si as a substrate material has been to lower the cost and weight of efficient GaAs solar cells. A major reduction in cost would be achieved if such cells could be produced either on inexpensive Si sheets currently being developed for low-cost Si cells⁵ or on thin Si films (~1 μm) being investigated for integrated circuit use.⁶ However, previous attempts to grow GaAs epilayers directly on Si by CVD have been largely unsuccessful because of difficulties in nucleation. As previously proposed,^{3,4} we have overcome these difficulties by coating Si substrates with a thin epitaxial film of Ge before GaAs deposition. Since Ge and GaAs have almost the same lattice constant (about 4 percent greater than that of Si), this procedure also has the advantage of locating the lattice mismatch at the Ge-Si interface, away from the GaAs layer.

The crystalline quality of the GaAs layers depends strongly on the quality of the Ge layers. Of several preparation techniques that were investigated, vacuum evaporation⁷ was found to yield the best Ge layers. In this technique, a p⁺ Si substrate oriented 2° off (100) towards {110} is maintained at a temperature of 550°C while the Ge is deposited to a thickness of 0.1 to 0.2 μm in about 2 min. The Ge films have mirror-smooth surfaces and have been shown to be epitaxial by electron and x-ray diffraction techniques. Transmission electron microscopy (TEM) of the films revealed microtwins and a dense network of misfit dislocations (~10¹³ cm⁻²) at the Ge-Si interface. In the Ge films the dislocation density is ~10⁹ cm⁻².

Epitaxial GaAs layers were deposited in an AsCl₃-GaAs-H₂ system² at 680°C on the Ge-coated Si substrates. Each layer consists of n⁺ (S, 4 × 10¹⁸ cm⁻³), p (Zn, 1 × 10¹⁶ cm⁻³), and p⁺ (Zn, 8 × 10¹⁸ cm⁻³) regions that are respectively 0.15, 2.0, and 4 to 12 μm thick. A secondary-electron micrograph of a cleaved and stained GaAs shallow-homojunction structure grown on Ge-coated Si is shown in Fig. III-1. The surface is mirror smooth, although the GaAs layers contain a few cracks parallel to {110} cleavage planes. Ion channeling measurements show that these layers are of excellent crystal quality. Figure III-2 is a 2-MeV ⁴He⁺ ion channeling spectrum of an 8-μm GaAs layer on a Ge-coated Si substrate. The minimum surface yield is 4 percent, equal to the value for epilayers on GaAs substrates. TEM observations indicate that there are no microtwins in the GaAs layers, and that the dislocation density is about 10⁷ cm⁻², two orders of magnitude lower than the density in the Ge films.

The fabrication techniques used for the solar cells were similar to those used for GaAs cells on single-crystal Ge substrates.² The thickness of the n⁺ layer was reduced from its initial value of 1500 Å to about 500 Å by alternating anodic oxidation and oxide removal steps. The last of these steps was an anodization that formed an oxide layer about 850 Å thick to serve as an antireflection coating. The cell areas ranged from 0.2 to 9.3 mm².

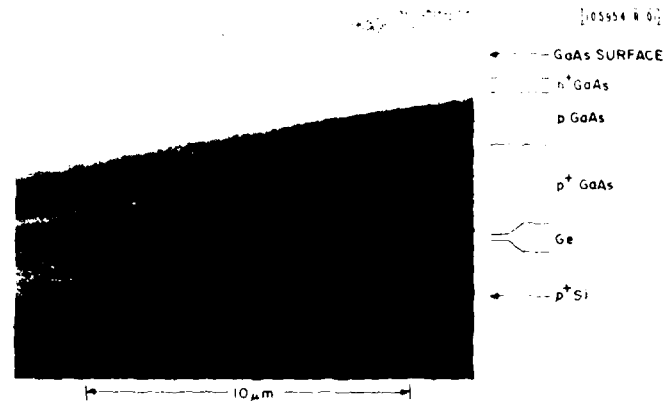


Fig. III-1. Secondary-electron micrograph of an 8- μm -thick GaAs shallow-homojunction structure grown on a Ge-coated Si substrate. The cleaved and preferentially etched sample was tilted 45° to allow both the upper GaAs surface and the cleaved edge to be seen.

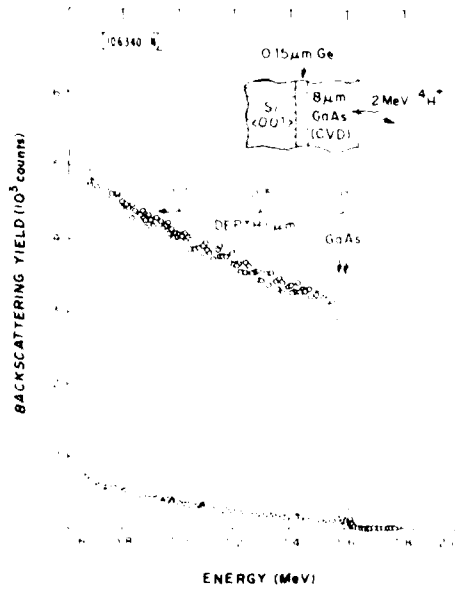


Fig. III-2. $^4\text{He}^+$ ion channeling spectrum for an epitaxial GaAs layer grown by CVD on a Ge-coated Si substrate.

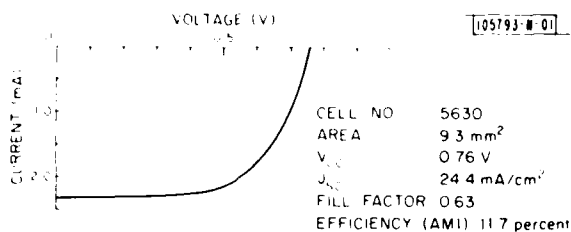


Fig. III-3. Photocurrent (at AM1) as a function of voltage for a GaAs cell on Ge-coated Si.

Figure III-3 shows the current-voltage curve obtained under simulated AM1 illumination at room temperature for the best 9.3-mm² GaAs cell on Ge-coated Si. The open-circuit voltage V_{OC} is 0.76 V, the short-circuit current density J_{SC} is 24.4 mA/cm² (not corrected for contact finger area), and the fill factor is 0.63, giving a measured efficiency of 11.7% (AM1). In comparison, our best cells on single-crystal Ge and GaAs substrates have V_{OC} of 0.94 V, J_{SC} of 25 mA/cm², and fill factor of 0.82 at AM1 (Ref. 2).

The external quantum efficiency of the cell of Fig. III-3 is plotted as a function of wavelength in Fig. III-4, along with values for one of our best cells on a GaAs substrate. The efficiency values for the cell of Fig. III-3 are the same at wavelengths up to 0.7 μ m and only 10 to 20 percent lower at the longer wavelengths. The relative decrease at the longer wavelengths indicates a shorter effective minority carrier diffusion length in the p region.⁸ Recombination at dislocations probably contributes to this shorter diffusion length, since images of the cell of Fig. III-3 obtained by the electron beam induced current (EBIC) technique (Fig. III-5) contain dark spots and lines that have the same density and morphology as the dislocations identified by TEM.

To investigate the diode properties of the junction in the cell of Fig. III-3, the dependence of J_{SC} (corrected for the contact finger area) on V_{OC} was determined by measurements at different illumination levels up to about 15 suns, with the cell mounted on a copper block maintained at 25°C. The diode factor and saturation current density were determined to be 1.7 and 6×10^{-11} A/cm², respectively. These values indicate that the reductions in V_{OC} and fill factor are the result of increased leakage current at the junction.

Figure III-6 is a schematic diagram summarizing the dislocation densities determined by TEM for the GaAs-Ge-Si structure. Misfit dislocations generated at the Ge-Si interface result in threading dislocations that propagate up through the Ge film. The GaAs-Ge interface acts as a barrier to these dislocations, the majority of which bend over and become part of a dislocation network at this second interface, where the mismatch is about 0.1 percent. The reduced junction quality of the solar cells on Ge-coated Si substrates, which is the reason for their lower efficiency, is probably due to the presence of dislocations at the junction. The dislocations may act as recombination centers, increasing the junction leakage current and thus lowering the diode factor, V_{OC} , and fill factor. This effect may be compounded by the bending over of dislocations at or near the junction, as seen in EBIC and TEM micrographs. Improvement in junction quality may therefore be achieved by reducing the overall dislocation density in the GaAs or by preventing dislocations from bending parallel to the junction.

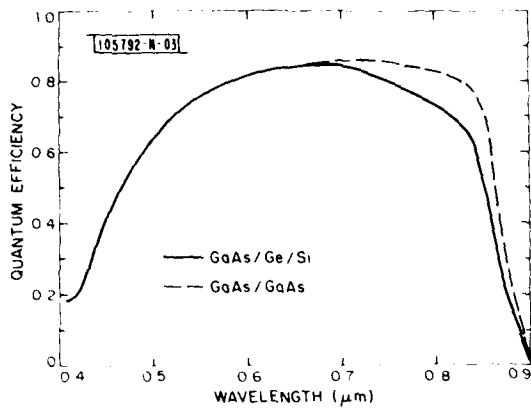


Fig. III-4. External quantum efficiency as a function of wavelength for the cell of Fig. III-3 (solid line) and for one of our best cells on a GaAs substrate (dashed line).

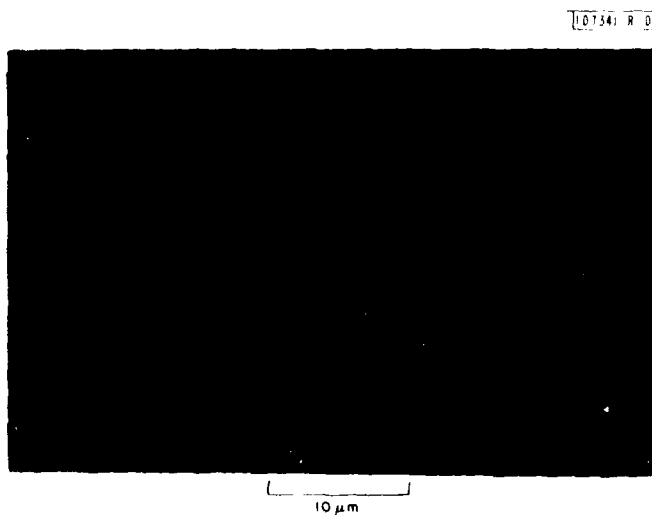
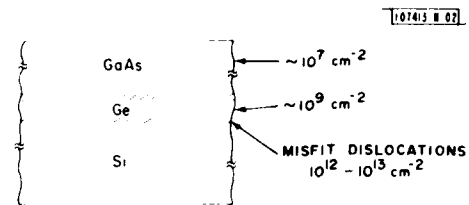


Fig. III-5. EBIC micrograph of a section of the cell of Fig. III-3 showing recombination at dislocations (short dark lines) and a crack in the epilayer (vertical dark line). Excitation was with 10-keV electrons.

Fig. III-6. Schematic of the GaAs/Ge/Si cross section summarizing the dislocation densities measured by TEM.



A second characteristic of the GaAs layers is the presence of cracks, which are formed because the linear thermal expansion coefficient of GaAs is roughly twice that of Si, so that the layers are placed under tensile stress by the substrate during cooling from the growth temperature. The most serious effect of the cracks occurs during the cell fabrication procedure. The junction will be shunted if p-GaAs exposed by a crack is electroplated with Sn during formation of the upper contact to the n⁺ region. This apparently occurred for several cells. However, many of the 9.3-mm² cells with good photovoltaic properties, including the cell of Fig. III-3, had one or more cracks crossing the mesa. Since the best of these cells had values of V_{oc} as high as those for devices without cracks, the cracks may not have a significant effect on V_{oc} . In addition, EBIC results indicate that J_{sc} is not reduced by proximity to a crack.

For the GaAs solar cells fabricated on Ge-coated Si substrates, the J_{sc} values are only slightly below the values for our best cells on GaAs and Ge substrates. Higher values of V_{oc} and fill factor will require improved junction characteristics, which we expect to achieve by further development of the technique for epitaxial growth of GaAs on Si.

R. P. Gale F. M. Davis
 B-Y. Tsaur G. W. Turner
 J. C. C. Fan

B. CATHODOLUMINESCENCE ANALYSIS OF POLYCRYSTALLINE GaAs

The utilization of polycrystalline GaAs for low-cost solar cells is not yet practical because the grain boundaries (GBs) in this material have adverse effects on device performance. With the objective of developing procedures to reduce these effects, we are investigating localized variations in the optoelectronic properties of polycrystalline GaAs associated with GBs and the effect of these variations on the performance of devices fabricated in polycrystalline GaAs. In an earlier study⁹ we demonstrated the effectiveness of infrared electroluminescence imaging for qualitative characterization of individual GBs in heavily doped GaAs. In this report we describe the application of cathodoluminescence (CL) analysis to polycrystalline GaAs. By collecting the CL emitted from a semiconductor specimen excited by the electron beam of a scanning electron microscope (SEM), CL analysis permits nondestructive evaluation of potential materials for photovoltaic devices without the necessity for charge-separating junctions or ohmic contacts. This technique can be used for local measurements of carrier concentration and diffusion length with spatial resolution of the order of 1 μ m, as well as for the imaging of spatial variations in radiative recombination by means of scanning CL microscopy (SCM). The observation of GBs in GaAs by SCM has recently been reported by McPherson *et al.*,¹⁰ but these workers made no detailed study of the CL properties.

The material examined in this study was heavily Zn-doped ($p \sim 10^{19} \text{ cm}^{-3}$), Bridgman-grown polycrystalline GaAs. Interest in this particular material was prompted by its use as the substrate for 13% (AM1) efficient shallow-homojunction solar cells prepared by chemical vapor deposition.¹¹

Slices of GaAs were lapped and polished to a thickness of 125 μm and sawed into squares 2.5 mm on a side. Samples containing GBs with various surface morphologies were selected for SCM analysis. All experiments were performed with the sample at ambient temperature in an SEM capable of supplying accelerating potentials ranging from 0 to 50 kV. The CL collection is accomplished with an optical microscope whose objective lens is coaxial with the incident electron beam. SCM imaging is accomplished by replacing the microscope eyepiece with a photomultiplier assembly, while spectral analysis is performed by directing the light onto a grating spectrometer with a resolution of 1 nm. All SCM and SEM images presented here were taken with a 30- or 35-keV electron beam at normal incidence. Carrier concentration determinations were made by spot-mode spectral full-width-at-half-maximum measurements at 30 kV using the data of Cusano.¹² Diffusion lengths were determined by measuring the CL intensity at 930 nm as a function of accelerating potential from 15 to 50 kV and curve fitting these data to a CL spectral theory recently developed by Vaughan.¹³

Figure III-7 compares SCM and SEM micrographs of the same sample area and demonstrates the capability of SCM to reveal defects not visible by surface microscopy of polished material. We have found that GBs can show three different types of CL contrast. These are illustrated in the SCM micrograph of Fig. III-7, where boundary A exhibits dark-line contrast, boundary B is slightly brighter than the surrounding matrix, and the two boundaries designated C show essentially no contrast, except for irregularly spaced dark spots that may be



Fig. III-7. SCM and SEM micrographs of the same polycrystalline GaAs sample. The GBs designated by A, B, and C exhibit three types of CL contrast.

precipitates. Note the bright regions running along both sides of boundary A. Most, but not all, of the boundaries appearing as dark lines showed this feature. The strong dark boundary to the upper left of C does not appear in the SEM image. The network structure at the upper left of the SEM micrograph is probably a dislocation network, perhaps associated with a sub-grain boundary.

Several additional features have been observed by SCM of polycrystalline GaAs. First, GBs with similar surface morphologies can have quite different CL properties. This is illustrated in Fig. III-8, where boundary A shows dark-line CL contrast while boundary B shows little or no contrast, although their SEM images are similar. Second, anomalous bright areas appear in many SCM images, such as those labeled C in Fig. III-9. In this figure they are associated with boundaries that show no CL contrast. In addition, it has been observed that the CL properties of a boundary can change substantially along its length. The following results indicate that these features are associated with variations in impurity concentration.

In Fig. III-9, the prominent curved boundary displays dark-line contrast, although the CL from the adjacent bright region is of such intensity that the dark line is barely visible. Carrier concentration and diffusion length were measured at point A in the adjacent bright region and at point B located 50 μm further into the grain. At A the carrier concentration is $9 \times 10^{18} \text{ cm}^{-3}$ and the diffusion length is 1.2 μm , while at B the respective values are $2 \times 10^{19} \text{ cm}^{-3}$ and 0.6 μm . The CL intensity vs accelerating potential data used to calculate these diffusion lengths are given in Fig. III-10.

These results suggest that dopant impurities are depleted from the bright regions bordering the GB and that these impurities are concentrated at the GB itself. Carrier concentration and diffusion length measurements made at other bright features, such as those denoted by C in Fig. III-9, are consistent with this interpretation. There was no measurable variation in carrier concentration and diffusion length associated with no-contrast boundaries.

The CL results indicate that both defect structure and impurity effects influence the optoelectronic properties of GBs in GaAs. Grain boundaries that show no CL contrast are believed to have little misfit between adjoining grains. Consistent with this idea, TEM has shown these defects to be $\{111\}$ twin boundaries with no observable dislocation structure. Figure III-11 is a TEM micrograph of a no-contrast boundary, obtained with the boundary parallel to the incident electron beam. The crystallographic relationships indicated in the figure are characteristic of a twin boundary.

Bright boundaries are probably twin boundaries where the impurity concentration in the adjacent regions has been reduced by segregation to the boundaries. The GBs exhibiting dark-line contrast are probably high-misfit boundaries. Although nonradiative recombination can be expected to occur at the misfit defects, this effect is insufficient to account for the observed darkening, since the width of the dark lines (typically 2 to 3 μm) is much greater than the width of the GBs themselves. Both an increase in impurity concentration and the formation of impurity precipitates probably contribute significantly to the reduction in CL intensity along these boundaries. These interpretations are summarized in Table III-4.

We believe that a close correlation will be found between the CL properties of GBs in GaAs and the effects of the GBs on the properties of photovoltaic devices. Thus, it seems likely that boundaries showing no CL contrast are electrically inactive and will not have a significant effect on device characteristics. Boundaries that appear dark have associated nonradiative recombination centers that can be expected to reduce short-circuit current and increase series

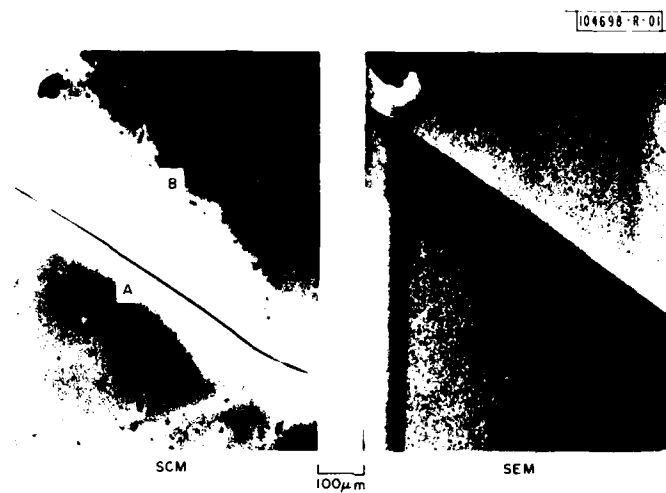


Fig. III-8. SCM and SEM micrographs of the same GaAs sample. Boundaries A and B show different CL contrast but similar surface morphologies.

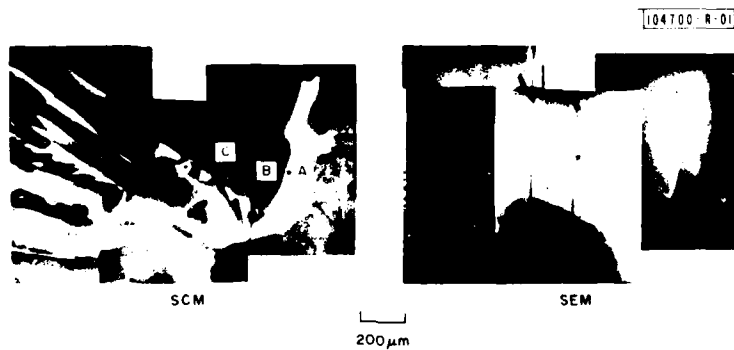


Fig. III-9. SCM and SEM composite micrographs of the same GaAs sample. The CL contrast results from local variations in impurity concentration. Carrier concentration and diffusion length measurements were made at A and B.

Fig. III-10. CL intensity vs accelerating potential measured at location A (near boundary) and B (crystal) in Fig. III-9. Each curve is normalized to the intensity at 30 kV.

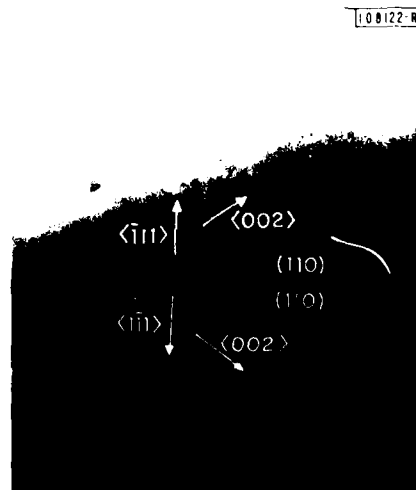
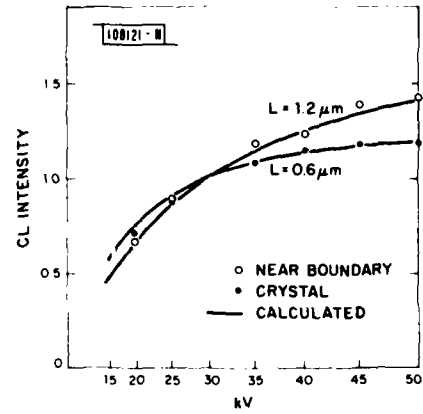


Fig. III-14. Transmission electron micrograph of a no-contrast GB in GaAs. The crystallographic orientations identify this as a twin boundary.

TABLE III-1 CATHODOLUMINESCENCE CONTRAST OF GRAIN BOUNDARIES IN GaAs		
Boundary SCM Image	Proposed Contrast Mechanism	
	Boundary Structure	Impurity Effects
No Contrast	Twin Absence of localized defects	No
Bright	Twin	Yes
Dark	High density of localized misfit defects	?
Dark With Bright Border	High density of localized misfit defects	Yes

resistance. Such boundaries that cross a device junction can cause a reduction in open-circuit voltage and fill factor. In addition, impurities concentrated along GBs could diffuse into epitaxial layers grown on heavily doped substrates, affecting device performance by altering band-gap states at the grain boundary or by changing the doping of the device structure. These effects are consistent with the low open-circuit voltages commonly observed for polycrystalline GaAs solar cells.

J. P. Salerno
R. P. Gale
J. C. C. Fan

C. TRANSIENT ANNEALING OF ARSENIC-IMPLANTED SILICON USING A GRAPHITE STRIP HEATER

In this report we describe the utilization of a simple graphite strip heater for transient annealing of ion-implantation damage in Si. Good electrical activation of As-implanted Si has been achieved by annealing for only 10 s, with results comparable to those obtained by conventional furnace annealing at 1000°C for 30 min.

A variety of transient annealing techniques have been used previously to induce solid-phase recrystallization of ion-implanted Si layers. Annealing by these techniques, for periods of only a few milliseconds to a few seconds, is essentially equivalent to conventional furnace annealing. Our objective has been to develop an extremely simple method for transient annealing that can process large-area samples without using a vacuum setup.

Single-crystal 10- Ω cm p-type <100> Si wafers were implanted at room temperature (RT) or liquid-nitrogen (LN₂) temperature in a nonchanneling direction with 120-keV As⁺ ions to doses of 5×10^{14} , 2×10^{15} , or 1×10^{16} cm⁻². Amorphous implanted layers were produced in all cases. The wafers were cut into 1- \times -1-cm samples that were annealed using the graphite strip heater shown schematically in Fig. III-12(a). The graphite strip with dimensions of 0.1- \times -4- \times -7 cm was firmly clamped to metal electrodes, and a chromel-alumel thermocouple imbedded in the center of the strip was used to monitor the temperature. The Si sample was

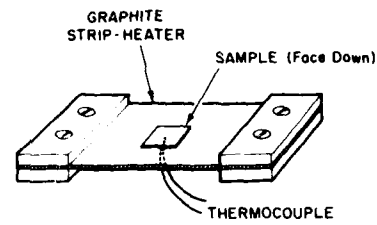
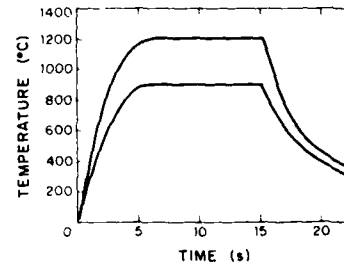


Fig. III-12. (a) Schematic diagram showing the experimental setup used for transient annealing of As-implanted Si. (b) Time-temperature profiles of two representative annealing runs.



placed at the center of the strip with the implanted side facing down. Annealing was performed in a flowing forming gas (Ar/H_2) ambient. The graphite strip was rapidly heated by passing an AC current of up to 350 A, and a microprocessor controller with digital input was used to control the current and hence the time-temperature profile. Figure III-12(b) shows two representative profiles, each with a rise time of ~ 5 s, a period of ~ 10 s at a maximum temperature, and a cooling rate of 100 to $200^\circ\text{C}/\text{s}$. Maximum temperatures ranging from 700 to 1200°C were used. To provide a comparison with the results of conventional furnace annealing, several implanted samples were annealed in a tube furnace at 1000°C for 30 min.

Crystallization of the implanted layers was accomplished by strip-heater annealing at maximum temperatures as low as 700°C . Backscattering experiments with $2\text{-MeV } ^4\text{He}^+$ ions were performed both at random incidence and with the samples aligned for $\langle 100 \rangle$ channeling. Figure III-13 shows random and aligned spectra for as-implanted, strip-heater-annealed, and furnace-annealed samples implanted at LN_2 temperature with an As dose of $2 \times 10^{15} \text{ cm}^{-2}$. The data for backscattering from Si atoms (energies less than 1.2 MeV) indicate that recrystallization of the amorphous layers was complete in both annealed samples, resulting in a minimum channeling yield of 3.8 percent. The channeling yield from As atoms (energies above 1.4 MeV) is also very low for these samples, indicating that over 98 percent of these atoms were present in substitutional sites. For the as-implanted sample, the peak concentration of As atoms determined from the backscattering data is $2 \times 10^{20} \text{ cm}^{-3}$, as predicted from ISS range statistics.¹⁴ The data for the strip-heater-annealed sample do not reveal any change in the distribution of As atoms, but pronounced redistribution occurred for the furnace-annealed sample. The marked difference, which has been confirmed by SIMS measurements, is expected because diffusion lengths of 18 and 950 Å are estimated for the strip-heater-annealed and furnace-annealed samples, respectively.

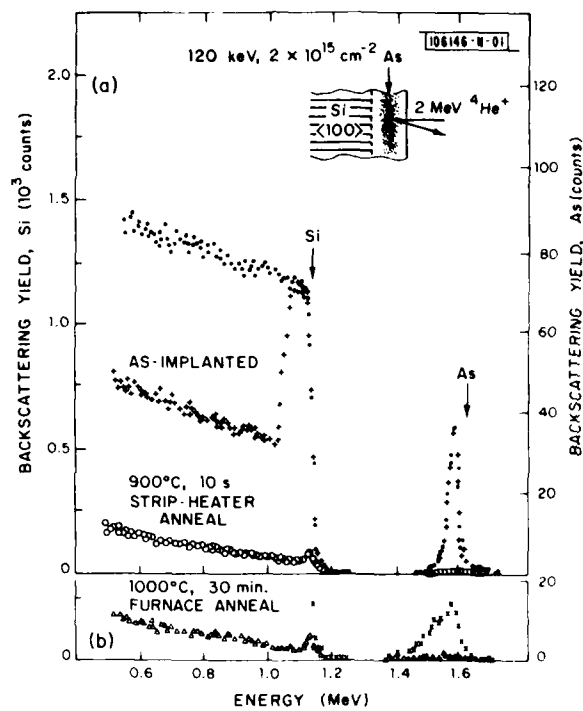


Fig. III-13. Backscattering spectra for Si samples implanted with $2 \times 10^{15} \text{ As}^+ \text{ cm}^{-2}$: aligned (○) spectrum for an as-implanted sample, random (●) and aligned (○) spectra for a sample that was strip-heater annealed at 900°C for 10 s; random (x) and aligned (○) spectra for a sample that was furnace annealed at 1000°C for 30 min.

Channeling measurements on samples implanted with a dose of $1 \times 10^{16} \text{ cm}^{-2}$ showed that only about 84 percent of the As atoms occupied substantial sites after strip-heater annealing at 1000°C for 10 s. The percentage of substitutional atoms was reduced because the peak concentration for this dose, $\sim 1 \times 10^{21} \text{ cm}^{-3}$, exceeds the equilibrium solubility of As in Si at 1000°C , $\sim 3 \times 10^{20} \text{ cm}^{-3}$ (Ref. 15). In a furnace-annealed sample, over 94 percent of the implanted atoms were found to be substitutional. The increase in substitutional percentage compared to strip-heater-annealed samples can be attributed to the diffusion that took place during furnace annealing, which reduced the fraction of As atoms that were present at concentrations exceeding the solubility.

The results of sheet-resistance measurements on all the annealed samples are shown in Fig. III-14. For strip-heater-annealed samples implanted with 5×10^{14} or $2 \times 10^{15} \text{ cm}^{-2}$, with increasing annealing temperature the sheet resistance decreases gradually to values approximating those of furnace-annealed samples. For a dose of $1 \times 10^{16} \text{ cm}^{-2}$, the sheet resistance values for strip-heater-annealed samples are higher than those for furnace-annealed samples, because of the lower percentage of substitutional As in the former. Strip-heater annealing at 1100 or 1200°C results in a decrease in sheet resistance, which can be explained by an increase in the substitutional percentage due to As diffusion. The lowest sheet resistance achieved is $22 \text{ m}\Omega$.

Surface Hall measurements have confirmed the effectiveness of strip-heater annealing. For doses of 5×10^{14} or $2 \times 10^{15} \text{ cm}^{-2}$, the sheet carrier concentrations and average mobility measured for strip-heater-annealed samples were generally close to those for furnace-annealed samples. For a dose of $1 \times 10^{16} \text{ cm}^{-2}$, the strip-heater-annealed samples have slightly lower values than furnace-annealed samples, consistent with the results of Fig. III-14.

Figure III-15 shows the forward I-V characteristics of a typical unpassivated mesa diode fabricated from a strip-heater-annealed sample. The sample had been implanted at RT with $1 \times 10^{16} \text{ cm}^{-2}$ As and annealed at 900°C for 10 s. The diode is $500 \mu\text{m}$ in diameter and has a $1 \mu\text{m}$ contact diameter. The forward characteristics are typical of near-ideal Schottky diodes. For over four orders of magnitude the characteristics can be fitted to the expression $I = I_0 [\exp(qV/kT) - 1]$ with $n = 1.1$, indicative of current flow dominated by minority carriers. At low forward bias, the characteristics can be fitted to the same expression with $n = 2.1$. This behavior is consistent with current generation in the space charge region, but it could also be due to surface leakage, since the diodes are unpassivated. Beyond 10^{-4} A the current deviates from the $n = 1.1$ line due to excess diode resistance. The reverse current is of the order of $\sim 10 \text{ nA}$ at -10 V , and the breakdown voltage exceeds $\sim 150 \text{ V}$.

The characterization results show that transient annealing with a simple graphite strip heater can induce solid-phase epitaxial recrystallization of As-implanted amorphous Si layers. Although the time at maximum temperature was set at 10 s in the present experiments, even shorter times should be sufficient. Complete activation of the implanted As, with negligible concentration, has been achieved for concentrations below the equilibrium solubility limit. The graphite strip heater can easily be scaled up for processing full-size wafers. The low cost of the experimental setup compared to laser or e-beam annealing equipment makes the strip-heater annealing technique attractive for semiconductor processing.

B.-Y. Tsaur J. C. C. Fan
J. P. Donnelly M. W. Geis

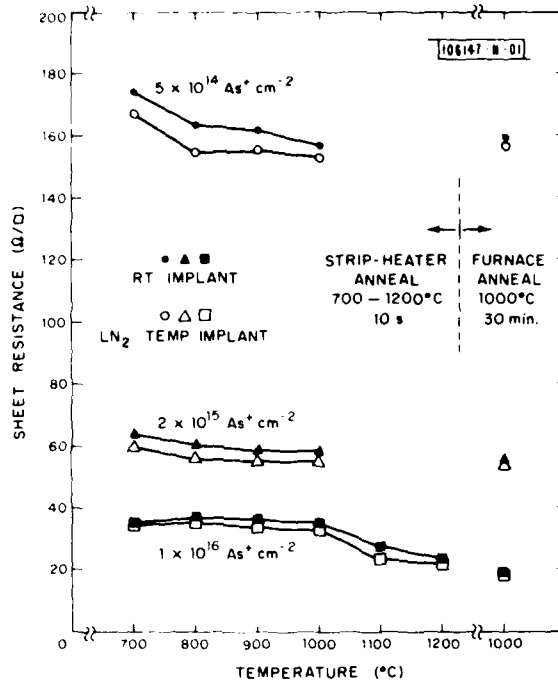


Fig. III-14. Sheet resistance of As-implanted Si samples after strip-heater annealing at 700 to 1200 °C for 10 s or furnace annealing at 1000 °C for 30 min.

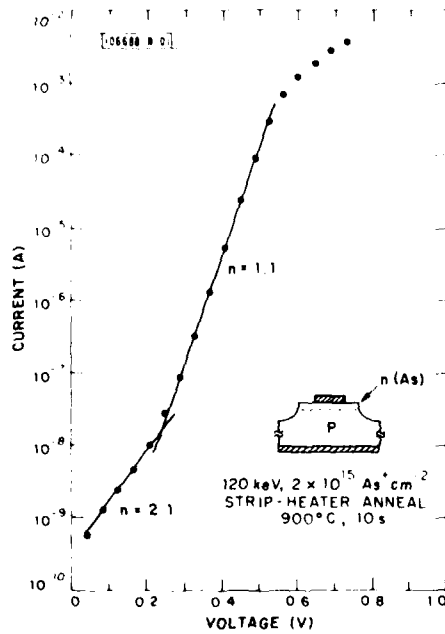


Fig. III-15. Forward I-V characteristics of an unpassivated mesa diode fabricated on a strip-heater-annealed sample.

D. SINGLE-CRYSTAL Si FILMS ON SiO₂ PREPARED BY USING A STATIONARY GRAPHITE HEATER FOR LATERAL EPITAXY BY SEEDED SOLIDIFICATION

Composite structures consisting of single-crystal Si films on insulators are of great interest for device applications. In recent experiments we prepared continuous single-crystal Si films on SiO₂ and Si₃N₄ by the technique of lateral epitaxy by seeded solidification (LESS).^{16,17} These experiments employed two graphite heaters, one of which was moved during LESS processing. In this report we describe the preparation of single-crystal Si films on SiO₂ by a new version of the LESS technique, which uses a single stationary graphite heater for transient heating. These films are comparable in crystal quality to those obtained by the two-heater procedure.

In the LESS technique, a single-crystal Si substrate is overcoated with an insulating layer, narrow stripes are opened to expose the substrate, and a thin film of amorphous or polycrystalline Si is deposited over the entire surface. The Si film is melted and frozen in such a manner that solidification initially occurs within each stripe opening, where it is seeded by the Si substrate, and then proceeds laterally over the adjacent insulating layer.

In our initial LESS experiments,^{16,17} the sample was placed face up on a stationary graphite strip-heater that was heated to about 1300°C. A movable graphite strip-heater, which was positioned about 2 mm above the sample, was raised to a temperature sufficient to melt a narrow zone of the Si film. Lateral epitaxy was accomplished by moving the upper heater at about 0.5 cm/s, causing the molten zone to move at the same rate. However, some observations made during these experiments indicated that lateral epitaxy could be achieved by transient heating even without moving the upper heater.

In the present investigation, <100> Si wafers 5 cm in diameter were masked with an SiO₂ film 0.2 μm thick formed by thermal oxidation. Stripes 3.5 μm wide and spaced 50 μm apart were opened in the SiO₂ film by standard photolithographic techniques. An amorphous Si film 0.6 to 0.7 μm thick was deposited in a chemical vapor deposition (CVD) reactor and capped with a CVD SiO₂ layer about 2 μm thick. The resulting structure is shown schematically at the lower left of Fig. III-16. Finally, rectangular samples with dimensions about 1 × 2 cm were cut from each wafer.

The upper part of Fig. III-16 shows the heater configuration used for LESS processing, which was performed in a flowing Ar ambient. The sample was placed on a graphite sheet with the Si film facing down. The graphite sheet was placed on a woven graphite cloth that was clamped between two electrodes. The low thermal mass of the graphite cloth allows rapid heating and cooling, and use of the graphite sheet greatly reduces the temperature variation across the sample. A typical time-temperature profile used for LESS processing is shown at the lower right of Fig. III-16. Stepped heating and cooling were used to prevent the formation of slip planes. With the time-temperature profiles used, any melting of the Si substrate was restricted to a thin surface layer.

In areas of the samples where stripes had been opened in the SiO₂ layer, LESS processing yielded continuous single-crystal Si films. In areas far from the openings, the films were polycrystalline, consisting of randomly oriented grains several hundred micrometers across. The characterization results indicate that solidification of the single-crystal films generally took place in the same manner as in the two-heater LESS experiments when the upper strip-heater was moved parallel to the long axis of the stripe-openings. In those experiments, seeded growth began within each opening and continued laterally over the insulating layer on

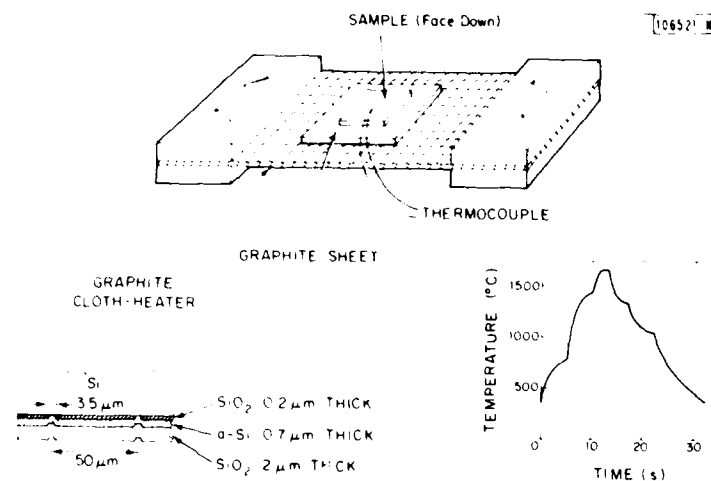


Fig. III-16. Schematic diagram showing the configuration used for the one-heater LESS technique. A cross-sectional diagram of a typical sample before LESS processing is shown in expanded form on the lower left. On the lower right is a time-temperature profile used for processing.

both sides of the opening until the growth fronts met the fronts originating from the two adjacent openings.

The Si films obtained were quite smooth, except for some surface features formed at the intersections of the growth fronts from adjacent openings. Such features are shown in Fig. III-17(a), which is an optical micrograph of an as-solidified film taken after removal of the SiO_2 cap. The linear features were found by TEM to be formed by dislocations, probably caused by a slight misorientation of the adjacent fronts. The circular features are dislocation clusters. In some areas, even delineation etching did not reveal intersections between adjacent fronts. In these areas, solidification of the film between adjacent openings probably took place by the motion of a single front that originated within one opening and moved to the other opening.

Optical micrographs of the Si films taken after etch delineation show the presence of a few microtwins that originate within the stripe openings and propagate along $\langle 110 \rangle$ directions over the SiO_2 layer, in some cases extending to the intersections between adjacent growth fronts. These twins, which are shown by TEM observations to be bordered by $\{111\}$ planes, are less than $0.5 \mu\text{m}$ wide and spaced a few hundred micrometers apart along the stripe openings.

As shown in Fig. III-17(a), the depressions in the Si film surface located over the stripe openings were retained during melting and solidification. This is also demonstrated by Fig. III-17(b), an SEM micrograph of a cleaved cross section of the sample of Fig. III-17(a) that had been etched with HF in order to delineate the SiO_2 mask. It is apparent that the mask retained its integrity during LESS processing. About half the $2\text{-}\mu\text{m}$ -thick SiO_2 cap remained after the HF etch. The Si film is about $0.6 \mu\text{m}$ thick. Other SEM micrographs show that the surface of the Si film outside the stripe openings is smooth except at the intersections between the growth fronts, where there are ridges a few hundred angstroms high.

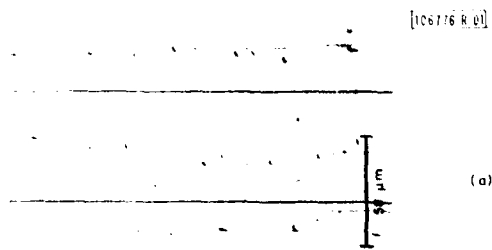
The quality of the Si films was confirmed by measurements of the Rutherford backscattering of $2\text{-MeV } ^4\text{He}^+$ ions. The diameter of the ion beam was about 1 mm , so that each measurement characterizes a region of the film produced by growth originating within about 20 stripe

openings. Figure III-18 shows the results of such a measurement made on the film of Fig. III-17 in an area where intersections between the fronts were observed. The open and closed circles show the spectra obtained when the beam was incident in a random crystallographic direction and in the $\langle 100 \rangle$ channeling direction, respectively. The minimum channeling yield at the surface (χ_{min}) is about 6 percent, not much higher than the value of 4 percent obtained for bulk single-crystal Si (also shown in Fig. III-18) and comparable to values measured for samples prepared by the two-heater LESS technique.¹⁷ The channeling yield increases to about 10 percent at the Si-SiO₂ interface. The dip in the random spectrum near 0.75 MeV is due to the presence of the SiO₂ mask, which has a lower Si concentration than elemental Si.

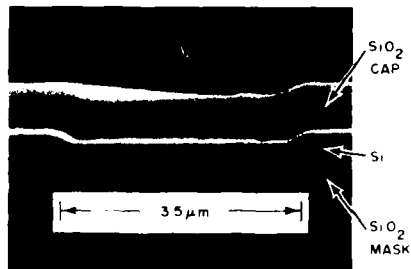
Figure III-18 also shows the channeling spectrum for the 0.6- μm -thick Si film of a commercial Si-on-sapphire (SOS) sample. While χ_{min} is only about 8 percent, the channeling yield increases to over 50 percent at the Si-sapphire interface, much larger than that at the Si-SiO₂ interface in the LESS sample. This indicates that the crystal quality is much better at the Si-SiO₂ interface than at the Si-sapphire interface.

In a number of preliminary experiments where the stripe openings were 250 μm apart, continuous single-crystal Si films were obtained, showing that lateral growth of at least 125 μm over SiO₂ can be achieved by the single-heater LESS technique. In fact, single-crystal overgrowth has been observed in some areas for distances up to 250 μm beyond the stripe openings. By optimizing the process parameters, including the temperature gradient in the plane of the sample and the rates of heating and cooling, it should be possible to significantly extend the distance of single-crystal growth.

J. C. C. Fan
B-Y. Tsaur
M. W. Geis



(a)



(b)

Fig. III-17. (a) Optical micrograph of a single-crystal Si film obtained by using the LESS technique of Fig. III-16; (b) SEM micrograph of a cross section of the same film.

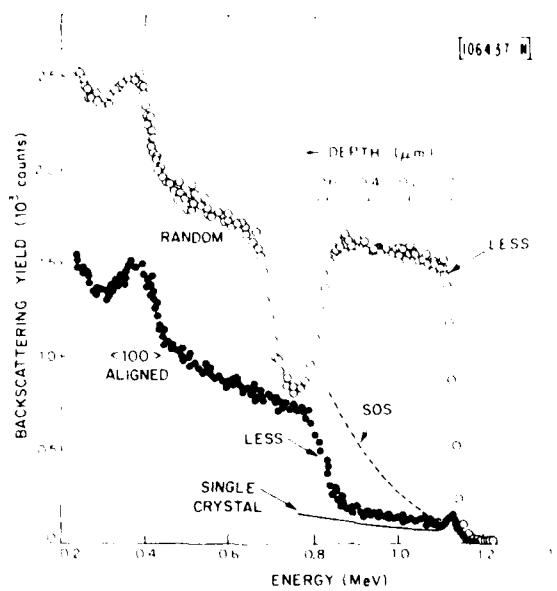


Fig. III-18. $^4\text{He}^+$ ion backscattering spectra for the LESS film shown in Fig. III-17. The open and closed circles show the spectra obtained when the ion beam was incident in a random direction and in the $\langle 100 \rangle$ channeling direction, respectively. The channeling spectra of a single-crystal Si wafer and a commercial Si-on-sapphire film are included for comparison.

REFERENCES

1. J. C. C. Fan, C. O. Bozler, and R. L. Chapman, *Appl. Phys. Lett.* 32, 390 (1978), DDC AD-A058281/7.
2. C. O. Bozler, J. C. C. Fan, and R. W. McClelland, Chapter 5 in Gallium Arsenide and Related Compounds (St. Louis) 1978 (The Institute of Physics, London, 1979), pp. 429-436, DDC AD-A072370/0.
3. J. C. C. Fan, C. O. Bozler, and B. J. Palm, *Appl. Phys. Lett.* 35, 875 (1979), DDC AD-A085504/5.
4. J. C. C. Fan, G. W. Turner, R. P. Gale, and C. O. Bozler, *Proc. Fourteenth IEEE Photovoltaic Specialists Conference - 1980, San Diego, California, 7-10 January 1980*, pp. 1102-1105, DTIC AD-A090668.
5. For a review, see P. D. Maycock, in Ref. 4, p. 6.
6. M. W. Geis, D. A. Antoniadis, D. J. Silversmith, R. W. Mountain, and H. I. Smith, *Appl. Phys. Lett.* 37, 454 (1980).
7. B-Y. Tsaur, M. W. Geis, J. C. C. Fan, and R. P. Gale, *Appl. Phys. Lett.* 38, 176 (1981).
8. H. J. Hovel, Solar Cells, Vol. 11 of Semiconductors and Semimetals (Academic Press, New York, 1975), p. 27.
9. G. W. Turner, J. C. C. Fan, and J. P. Salerno, *Solar Cells* 1, 261 (1980).
10. J. W. McPherson, W. Collis, E. Stefanakos, A. Safavi, and A. Abul-Fadl, *J. Electrochem. Soc.* 127, 2713 (1980).
11. G. W. Turner, J. C. C. Fan, R. P. Gale, and O. Hurtado, *Proc. Fourteenth IEEE Photovoltaic Specialists Conference - 1980, San Diego, California, 7-10 January 1980*, pp. 1330-1332, DTIC AD-A090294.
12. D. A. Cusano, *Solid State Commun.* 2, 352 (1964).
13. J. Vaughan, Ph.D. Thesis, M.I.T. (1981), unpublished.
14. J. F. Gibbons, W. S. Johnson, and S. W. Mylroi, Projected Range Statistics, 2nd Edition (Dowden Hutchinson and Ross, Stroudeburg, Pennsylvania, 1975).
15. L. Csepregi, E. F. Kennedy, S. S. Lau, J. W. Mayer, and T. W. Sigmon, *Appl. Phys. Lett.* 29, 645 (1976); L. D. Glowinski, K. N. Fu, and P. S. Ho, *Appl. Phys. Lett.* 28, 312 (1976).
16. J. C. C. Fan, M. W. Geis, and B-Y. Tsaur, *Proc. 1980 IEEE Intl. Electron Devices Mtg.*, Washington, D.C., 8-10 December 1980, p. 845.
17. J. C. C. Fan, M. W. Geis, and B-Y. Tsaur, *Appl. Phys. Lett.* 38, 365 (1981).

IV. MICROELECTRONICS

A. CHARGE-COUPLED DEVICES: IMAGERS

Satellite surveillance at the GEODSS (Ground-Based Electro-Optical Deep Space Surveillance) sites is currently confined to night viewing. Recently there has been interest in the possibility of extending surveillance into the daylight hours. However, the high-sky background adds a large noise to the signal and precludes the highly sensitive detection possible at night. Nevertheless, it appears that brighter, low-altitude satellites can be detected by current CCD sensors, and, in fact, these satellites are often difficult to observe at night because of occultation by the earth. In this report we describe evaluation of a technique called "charge skimming" which could be used to increase the sensitivity of a CCD sensor for the high-background imaging characteristic of daytime sky surveillance.

For a high-background, low-contrast imaging situation, the signal-to-noise ratio (SNR) at the output of a CCD will be $N_s / \sqrt{(N_B + N_s)} \approx N_s / \sqrt{N_B}$, where N_s and N_B are the number of photoelectrons per charge packet due to signal and sky background, respectively. This assumes that photon noise dominates the noise sources in the CCD, an assumption that is easily satisfied in practice. Because the daytime sky background is so large, a typical CCD would saturate on telescopes of about 15-in. diameter. One could attenuate the optical signal with neutral-density filters, but this would reduce the SNR by the square root of the attenuation. Thus, the challenge in using CCDs without sacrificing SNR is to increase the exposure level at which the devices saturate. This could be accomplished by increasing the charge capacity of the CCD pixels, or by decreasing the integration time (increasing the output data rate) while performing compensatory integration off-chip.

However, a more convenient technique for the low-contrast imaging situation discussed above is to perform in the charge domain a function similar to AC coupling. In this method a fixed quantity of charge resulting from the background is subtracted from the charge packet, and the small remaining portion containing the signal information is retained. Kosonocky and Sauer¹ have demonstrated this technique in a closed-loop CCD structure where it was used to remove dark current from the signal. We have studied this technique experimentally using the final stage in the output register of a two-phase CCD imager. Figure IV-1 describes the final transfer stage and illustrates the dynamics of charge flow involved in the skimming process. A charge packet under the ϕ_1 storage well (the rightmost of the two ϕ_1 gates) is transferred on the falling edge of the ϕ_1 clock to the ϕ_2 storage well. In normal operations the output gate would be biased to a DC potential lower than suggested by Fig. IV-1, so that all of the charge received by ϕ_2 would be retained until a half clock period later. When the ϕ_2 potential drops, the entire charge packet would be transferred to the output diode.

In Fig. IV-1, however, the output gate is shown biased to a level that permits a portion of the charge, Q_{SK} , to be skimmed off and transferred to the output diode. The residual charge Q_R is left in the ϕ_2 storage well and is subsequently transferred to the output diode on the falling edge of the ϕ_2 clock. In this experiment, Q_R represents a portion of the sky-background generated charge which we wish to discard, while the skimmed charge, Q_{SK} , may contain a signal and is saved.

PRECEDING PAGE BLANK-NOT FILMED

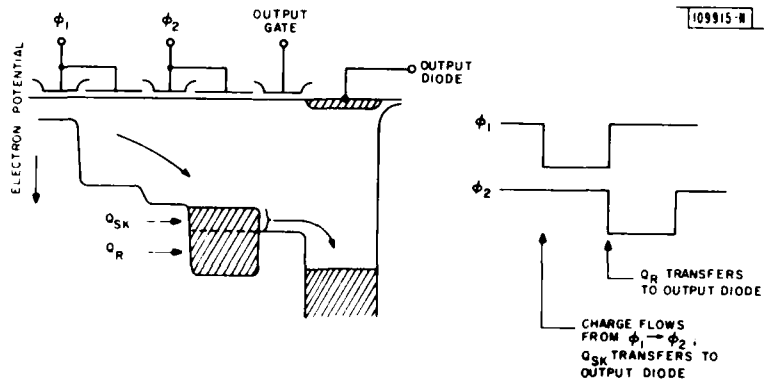


Fig. IV-1. Illustration showing the charge flow at the output of a CCD operated in a charge-skimming mode. The charge Q_{SK} is skimmed off as shown, and Q_R is the residual charge left under the output gate.

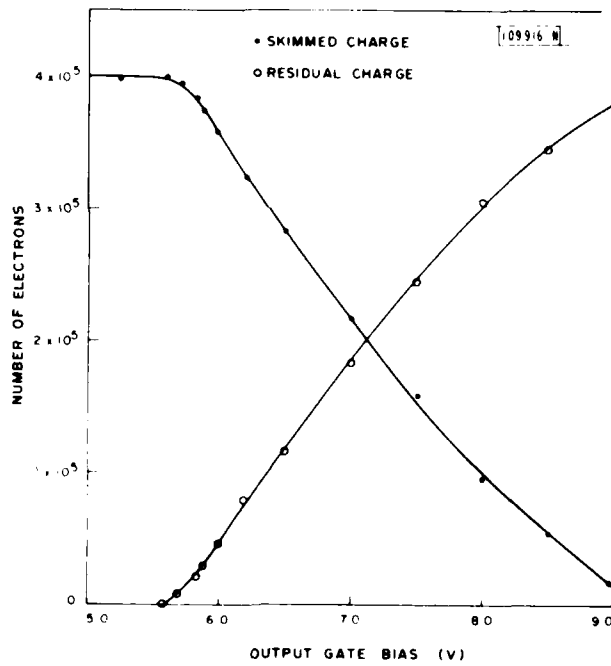


Fig. IV-2. Measurements of the skimmed and residual charge as a function of output gate bias.

This technique is useful when the very wide dynamic range signals of CCDs are to be processed by amplifiers and A/D converters of limited dynamic range. In addition, this structure (with modifications) could be incorporated into an imager pixel or column of pixels where it could be used to suppress the charge buildup from the background.

The charge-skimming process described in Fig. IV-1 has been demonstrated in two experiments. In the first we illuminated the output register to generate charge packets of approximately 400,000 electrons and measured the skimmed and residual charge as a function of output gate bias. These data, taken at a clock rate of 200 kHz, are plotted in Fig. IV-2 and show that the skimming commences at 5.60 V. Above 5.60 V, the slopes of the lines are proportional to the capacitance C of the ϕ_2 storage well:

$$C = (1/\beta) dQ_R/dV_{OG} = - (1/\beta) dQ_{SK}/dV_{OG}$$

where $\beta = 0.9$ is a factor representing the modulation of the electron potential in the channel by the output gate² and V_{OG} is the output gate bias. The values of C range from 27 fF at 5.9 V to 18 fF at 9 V, reflecting the changing depth of the charge centroid in the buried channel.

In the second experiment we simulated a low-contrast imaging situation by adding three small charge packets to the optically induced charge and measured their amplitude as a function of skimming. The charge packets, which were inserted electrically, are about 3,700 electrons, so that SNR = 5.9. The amplitude of the three signal packets as a function of output gate bias is plotted in Fig. IV-3, and, as expected, the signal is entirely skimmed off shortly after the onset of skimming. The oscilloscope photographs of Fig. IV-4 show the CCD output for the skimmed (upper trace in each photograph) and residual charge (lower trace) below and just above the skimming threshold. Figure IV-4(a), taken at a gate bias of 5.53 V, shows no signal in the skimmed charge, while the residual charge consists of the 3,700-electron signal riding on the 400,000-electron background (signals are negative-going in these photos). The photon noise of 530 electrons rms is evident in the lower trace. At 5.98 V [Fig. IV-4(b)], both the signal and the photon noise have been skimmed off, leaving behind a residual charge of 360,000 electrons (from Fig. IV-3). However, the residual charge also has a small noise component which is expected to be $\text{var}Q_R = \gamma kTC$, where C is the storage-well capacitance previously mentioned and γ is a factor close to unity.² The measured noise of 55 to 30 electrons agrees with theory for $\gamma = 1.4$.

An important detail of these experiments is that the rise and fall times of the ϕ_1 and ϕ_2 clocks were set to about 700 ns. When the rise and fall times were reduced to their normal values of 30 ns, the data of Fig. IV-3 showed a more gradual skimming extending over about 0.75 V. This suggests that the fast CCD clock transients are causing modulation of the substrate and output gate potentials, and are therefore preventing the output gate from cleanly "slicing" the charge packet in two. This effect places a limit on the maximum amount of skimming that can be done without attenuating signals that are not much larger than the photon noise. Most imager applications require high video data rates which preclude clock waveforms with slow rise and fall times. Therefore, the effectiveness of the skimming technique will depend on careful device design to minimize clock coupling to the skimming gate.

B. E. Burke

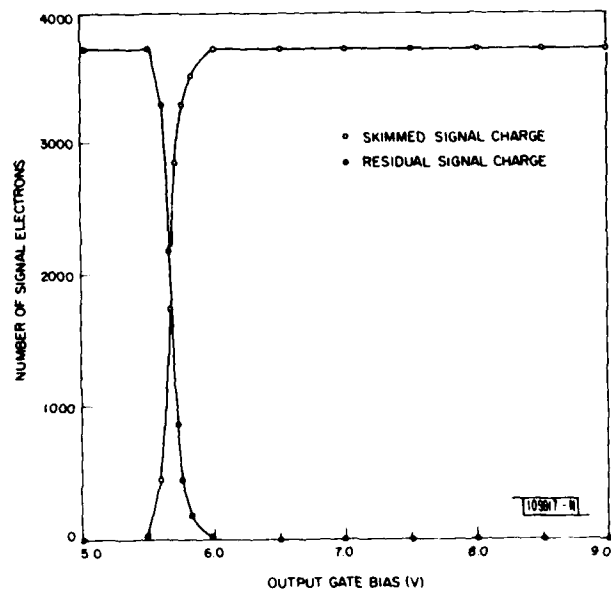
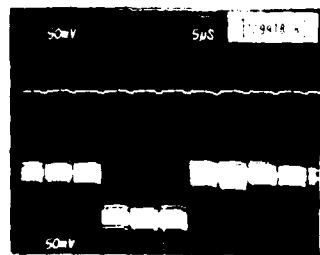


Fig. IV-3. Measurements of the electrically inserted 3,700-electron signal as it is skimmed off the 400,000-electron background charge.



(a)



(b)

Fig. IV-4. CCD output showing the skimmed (upper trace) and residual charge (lower trace) for three 3,700-electron packets riding on a 400,000-electron background (signal is negative-going). Output gate bias is 5.53 V in (a) and 5.98 V in (b).

B. OXIDE BARRIERS TO FORMATION OF REFRACTORY SILICIDES

In this report we discuss attempts to form refractory silicides using an alternating metalization technique. Results for WSi_2 , $MoSi_2$, and $TaSi_2$ indicate a different interdiffusion mechanism associated with the formation of WSi_2 than with the formation of $MoSi_2$ or $TaSi_2$ if gas phase impurities (probably oxygen) are incorporated in the deposited refractory film. These results are applicable to the fabrication of silicon device structures which use refractory metals on SiO_2 and silicon, such as the permeable base transistor.

Although doped polysilicon has been successfully utilized as a gate and interconnect metalization, the minimum obtainable sheet resistivity of $20 \Omega/\square$ for polysilicon is not adequate for many applications. To address this problem several refractory metal silicides³ have come under study. These materials offer the potential for sheet resistivities an order of magnitude less than doped polysilicon while retaining the same capability for lithographic processing, etching, and thermal self-passivation as polysilicon. WSi_2 , $MoSi_2$, and $TaSi_2$ have been identified⁴ as materials of particular interest because of high temperature stability, ease of formation, low bulk resistivity, and relative resistance to wet HF etchants. These films have been formed in a controlled fashion by electron-beam co-evaporation⁵ of metal and silicon and by co-sputtering from targets of the two metals.⁶ In this work, an alternating layer deposition technique⁷ developed for PtSi has been utilized for forming refractory silicides.

Substrates were prepared by depositing 600 \AA of low-pressure chemical-vapor-deposited (LPCVD) Si_3N_4 and 3000 \AA of phosphorus-doped LPCVD polysilicon onto silicon wafers with 5000 \AA of thermal oxide. By using a multi-hearth electron-beam evaporator, four alternating pairs of nominally 200-\AA -thick films of tungsten and 525-\AA -thick films of silicon were deposited to form composites whose composition was equivalent to stoichiometric WSi_2 . Similar four-pair depositions ($200 \text{ \AA} \text{ Mo}/525 \text{ \AA} \text{ Si}$ and $200 \text{ \AA} \text{ Ta}/460 \text{ \AA} \text{ Si}$) were performed for stoichiometric $MoSi_2$ and $TaSi_2$. The films were reacted and homogenized in a high-purity H_2 ambient at $950^\circ C$ for 30 min.

Four-point probe measurements showed sheet resistivities of $\approx 5.4 \Omega/\square$ for WSi_2 , $\approx 12.2 \Omega/\square$ for $MoSi_2$, and $2.8 \Omega/\square$ for $TaSi_2$. X-ray diffraction and Auger analysis confirmed that a mixing reaction had taken place for both the $MoSi_2$ and $TaSi_2$ films, but a distinct layer structure was retained for the W-Si composite structure despite the low sheet resistivity for these films. Although isolated regions of WSi_2 approximately $100 \mu m$ in size were observed, no uniform tungsten silicide films were formed until samples were annealed at temperatures greater than $1000^\circ C$.

To study the W-Si reaction further, silicon substrates were prepared with 20 \AA of thermal oxide followed by 300 \AA of electron-beam-evaporated tungsten and 800 \AA of electron-beam-evaporated silicon deposited without breaking vacuum. Auger sputtering analysis of these samples (Fig. IV-5) shows the distinct silicon substrate layer, the thin oxide, and the deposited silicon and tungsten layers. Since tungsten does not readily form a native oxide at low temperatures, the oxygen peak at the evaporated tungsten/evaporated silicon interface is somewhat surprising. However, this peak may be related to outgassing of the silicon source prior to silicon deposition as the vacuum integrity degrades during this process to approximately 10^{-6} Torr from a base pressure of 2×10^{-7} Torr.

After the above Auger analysis was completed, the substrates were annealed in a high-purity H_2 ambient for 30 min. at $1000^\circ C$ and a second Auger analysis was performed, the results of which are shown in Fig. IV-6. This analysis shows that no mixing has taken place, and

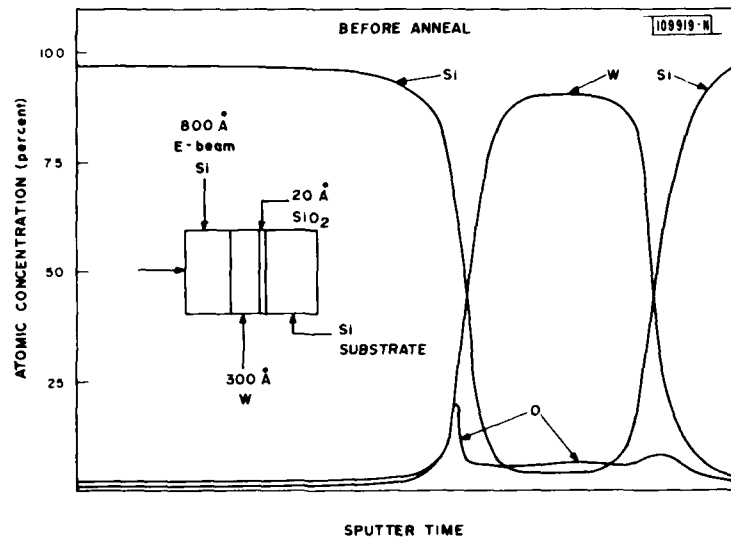


Fig. IV-5. Auger analysis of an electron-beam-evaporated W-Si composite film deposited on a Si substrate with a thin thermal/oxide.

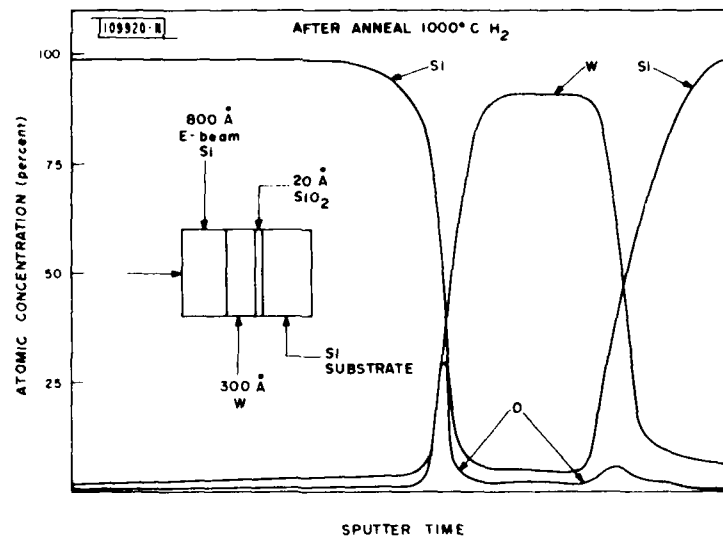


Fig. IV-6. Same as Fig. IV-5, except after 30 min. anneal in H₂ at 1000 °C.

the oxygen peak at the evaporated tungsten/evaporated silicon interface appears to have increased as shown in Fig. IV-7, which is an enlargement of the oxygen curve of Fig. IV-6. In addition, the level of oxygen in the tungsten film appears to have decreased. Although the chemical nature of the oxygen between the deposited tungsten and silicon films cannot be precisely determined, it is sufficient to prevent silicide formation at 1000°C, about 350°C higher than the reaction temperature for the uninhibited formation of WSi_2 .

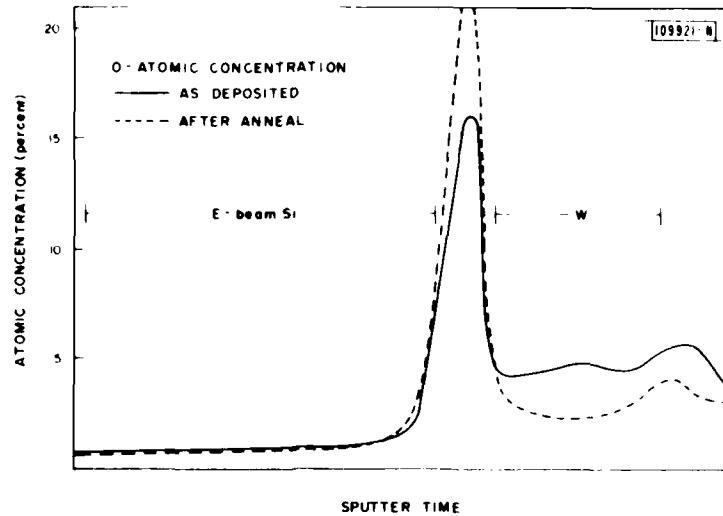


Fig. IV-7. Comparison of expanded oxygen peaks from Figs. IV-5 and IV-6 between electron-beam-deposited Si and W before and after H_2 anneal. The oxygen peak has increased after anneal, indicating the diffusion of oxygen from the bulk of the film to the W-Si interface.

A possible explanation for the results of these Auger analyses is that the tungsten film contains some level of oxygen due to the gettering of residual oxygen in the vacuum. In addition, the outgassing of the silicon source mentioned above may enhance the level of oxygen at the evaporated W-Si interface. When the composite layer is annealed at high temperatures in a H_2 ambient, the oxygen diffuses readily out of the bulk of the film to the interface probably forming SiO_2 , an oxide which is more stable than WO_3 . The resulting thin SiO_2 film has sufficient integrity to prevent silicon diffusion into the tungsten, thereby preventing WSi_2 formation.

In conclusion, the chemistry of vacuum-deposited tungsten films allows for the formation of an isolating layer of oxide if a silicon film is deposited over the tungsten layer. This oxide layer prevents the formation of WSi_2 at temperatures up to 1000°C. This mechanism does not occur for alternating Mo-Si or Ta-Si depositions. This unique property of tungsten makes it inherently useful for buried-metal films in silicon devices.

D. J. Silversmith
D. D. Rathman
R. W. Mountain

C. PATTERN REGISTRATION USING THE SCANNING ELECTRON BEAM LITHOGRAPHY SYSTEM

The scanning electron beam lithography system (SEBL) at Lincoln Laboratory has been applied to a variety of high-resolution writing tasks, including fabrication of diffractive optics⁸ and electronic devices.⁹ However, we have not previously fully developed and exploited the high-accuracy pattern registration capabilities of the SEBL. This report discusses the application of the SEBL to high-resolution alignments, and describes the alignment of FET device patterns with submicrometer feature sizes. Experimental results are presented.

The experiments in pattern registration utilized an ETEC LEBES-D SEBL. This is a vector scan machine with a 1-mm field size. The sample is mounted on a servo-controlled, x-y translation stage. The stage is used to step a pattern across the sample and to stitch together patterns which exceed the field size of the machine. The motion of the servo stage and the deflection of the electron beam are controlled in real time by a dedicated minicomputer. The minicomputer provides pattern generation capabilities, data storage facilities, and a convenient operator interface. The SEBL is equipped with a secondary electron detector which may be used to image the sample as in a conventional scanning electron microscope (SEM).

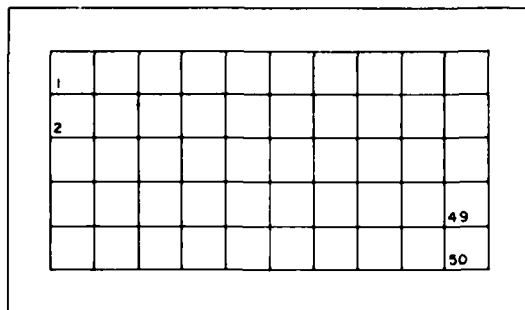
In principle, alignment to an existing pattern layer is quite simple using the SEBL. The operator, while viewing the SEM image of the sample, locates two or more alignment marks. Based upon the location of these marks, the minicomputer calculates the appropriate x-offset, y-offset, and rotation to be applied when the new pattern is written. Since the alignment marks can be greatly magnified in the SEM image of the sample, high-resolution alignment should be readily achieved.

However, the alignment procedure is complicated by several practical considerations. The highest accuracy alignment will require small alignment marks located close to the pattern area. Such marks are difficult to see at low magnification, and at high magnification the field of view is reduced to the point that searching for the marks is required. Since the SEBL will expose the resist in the area of observation when used to image the sample, indiscriminate hunting for the alignment marks may result in unwanted exposure in the pattern areas. Furthermore, the alignment marks themselves may be damaged as a result of exposure of the resist and subsequent processing steps.

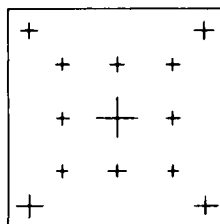
These difficulties can be avoided by using a multistep alignment procedure. The initial steps involve coarse registration to large alignment marks viewed with low magnification. These alignment marks must be well removed from the critical pattern areas to avoid unwanted incidental exposure. Further safeguards are provided by using the computer to coordinate stage motion and beam scanning. Once the coarse alignment has been accomplished, it is easy to find and image a set of small alignment marks at high magnifications which provides the high-resolution alignment. The fine-alignment step may be repeated at various areas on the sample to compensate for wafer distortion and electron-beam drift.

Figure IV-8 illustrates the layout of a GaAs substrate which has been used to test the alignment capabilities of the SEBL. The sample is divided into 50 fields, each 1 x 1 mm. Two fields in the upper left corner and one field in the lower right corner contain alignment crosses. The remaining fields each contain four submicrometer-gate FET device patterns. These devices are designed to have a 2- μ m source-drain spacing and a 0.5- μ m gate length. An optical micrograph of one such device pattern is shown in Fig. IV-9.

Fig. IV-8. Diagram of the layout of the fields on a GaAs substrate. Fields 1, 2 and 50 contain alignment patterns. The remaining fields contain FET device patterns.

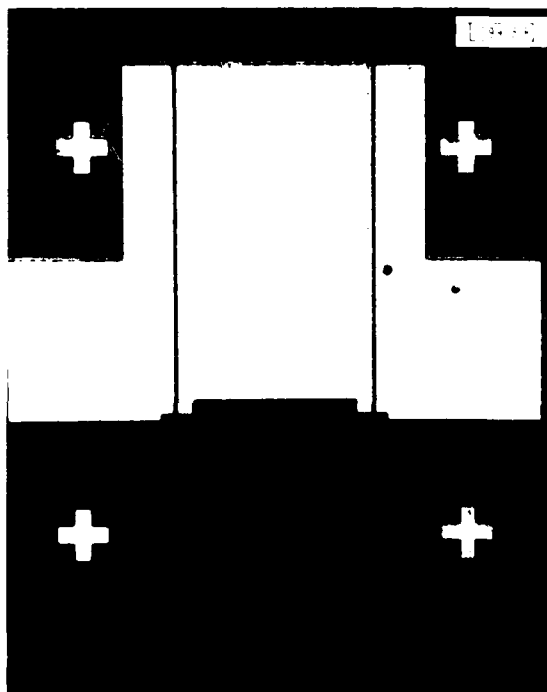


LAYOUT DIAGRAM



FIELD 1 DETAIL

109922-N



FET DEVICE PATTERN

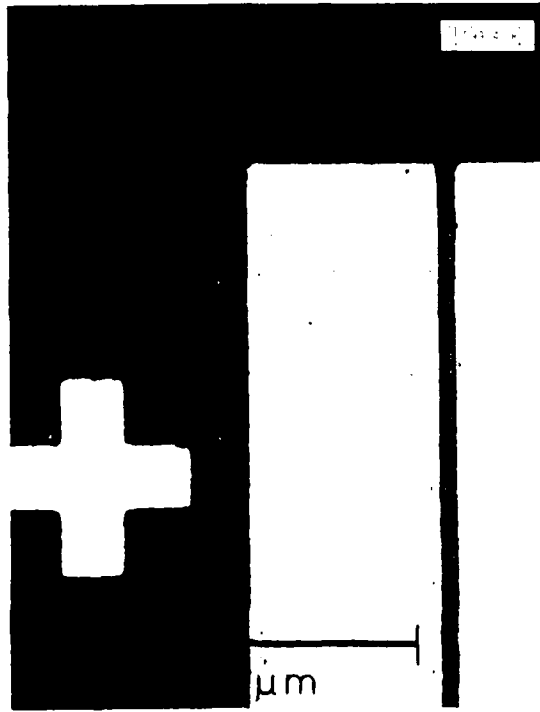
Fig. IV-9. Photomicrograph of a submicrometer-gate FET device.

The first lithographic step in the fabrication of the FET involves using the SEBL to pattern the source and drain ohmic areas and the alignment marks. These are the bright areas in Fig. IV-9. The Au-Ge metallization of the ohmic layer provides high-contrast alignment marks for use in the later steps. The alignment procedure begins when the sample is loaded into the SEBL and the upper left corner of the sample is imaged and located. The distance between the sample corner and the first pattern field was accurately established when the first pattern layer was written in the SEBL. Thus, finding the corner provides a convenient method for achieving the initial coarse alignment. In the next step, an alignment cross in field 1 is located. The computer generates a scan and a cursor, and the operator centers the cursor on the alignment cross by moving the scan field and the stage. The coordinates are then locked into the computer. These coordinates are used to determine the x-offset and y-offset of the sample. The accuracy of this measurement depends upon the electron-beam-probe size, the quality of the alignment mark, and the signal-to-noise ratio of the image. An accuracy of $\pm 0.3 \mu\text{m}$ is not difficult to obtain. A second alignment mark, also located in field 1, is used to determine the rotation. A third alignment mark, located in field 50, is used to refine the computation of the rotation. The alignment marks in field 2 are used as spares in case some of the other marks are damaged during the imaging. Field 2 also provides a readily apparent asymmetry to the sample, which simplifies orientation for loading.

The alignment procedure described above has been used to demonstrate $\pm 1\text{-}\mu\text{m}$ alignment across a $5 \times 10\text{-mm}$ sample. This is sufficient overlay accuracy for most of the pattern layers for the FET. The alignment of the $0.5\text{-}\mu\text{m}$ gates to the $2.0\text{-}\mu\text{m}$ source-drain opening will require maintaining a registration accuracy of $\pm 0.3 \mu\text{m}$. This will require aligning at each 1-mm field. Figure IV-9 illustrates a gate alignment. The bright areas are the Au-Ge from the first pattern layer. The gate pad, which is written in resist, appears as the light-gray structure in the micrograph. Notice the exposed resist over the alignment mark in lower right corner. The second mark which was used to align to this field is not visible in the micrograph. In Fig. IV-10 the upper left area of the device is illustrated at higher magnification. The $0.5\text{-}\mu\text{m}$ gate can be seen to be aligned to the source and drain regions.

The alignment procedures described in this report offer some exciting possibilities for device research at Lincoln Laboratory. Current efforts toward the fabrication of a submicrometer-gate FET center around developing processing and lithography. Work is also under way to improve and fully automate the alignment procedure.

T. Lyszczyarz
G. Lincoln
C. Smith



SUBMICRON GATE ALIGNMENT

Fig. IV-10. Photomicrograph of a submicrometer-gate FET showing the alignment of the gate to the source and drain ohmic regions.

REFERENCES

1. W. F. Kosonocky and D. J. Sauer, RCA Rev. 40, 241 (1979).
2. R. W. Brodersen and S. P. Emmons, IEEE J. Solid-State Circuits SC-11, 147 (1976).
3. S. P. Muraka, J. Vac. Sci. Technol. 17, 775 (1980).
4. S. P. Muraka, D. B. Fraser, A. K. Sinna, and H. K. Levenstein, IEEE J. Solid-State Circuits SC-15, 474 (1980).
5. S. Zirinsky, W. Hammer, E. D'Hearle, and J. Baglin, Appl. Phys. Lett. 33, 76 (1978).
6. R. S. Nowichi, Solid State Technology 23, 95 (1980).
7. Solid State Research Report, Lincoln Laboratory, M.I.T. (1981-1), p. 48.
8. D. C. Shaver, D. C. Flanders, N. M. Ceglie, and H. I. Smith, J. Vac. Sci. Technol. 16, 1626 (1979), DTIC AD-A090073.
9. Solid State Research Report, Lincoln Laboratory, M.I.T. (1980-2), pp. 33-36, DTIC AD-A092724.

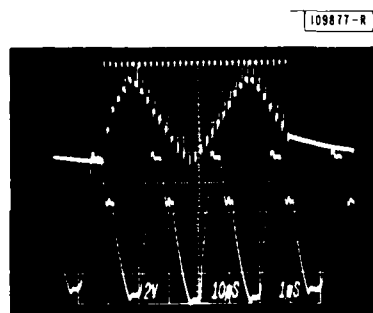
V. ANALOG DEVICE TECHNOLOGY

A. ANALOG MNOS MEMORY: SPEED AND ENDURANCE CAPABILITIES AND CORRELATOR PERFORMANCE

In previous reports,¹ theory and experiments related to the nonvolatile storage of analog signal levels in MNOS capacitors were presented. A recent report² described initial evaluation of the storage of sampled analog waveforms in MNOS/CCD structures. In the present contribution, recent tests exploring the capabilities of the existing MNOS/CCD device are presented, with emphasis on input/output speed, stored waveform retention, and endurance to erase/write cycling. In addition, the ability of the same device to perform binary/analog memory correlation is described.

With some changes made to lower the input capacitance of the off-chip output buffering circuit, the 32-sample memory operates well at 500-kHz input and output sample rates. Figure V-1 shows an entire output cycle (10 μ s/div) and a superimposed expanded view of several samples (1 μ s/div). Although the serial transfer inefficiency of the CCD itself is in the low 10^{-4} range at this speed, charge transfer through the long wells at the input circuit begins to contribute to sampling errors. In addition, the slow rate of the output circuit is being approached.

Fig. V-1. Readout of stored analog waveform at 500 kHz. Upper trace: entire train of 32 output samples, 10 μ s/div. Lower trace: expanded view of several output sample periods, 1 μ s/div.



The relationship between the number of erase/write (E/W) cycles a device has undergone and its charge retention is under investigation. Devices which have undergone more than 10^6 E/W cycles are capable of storing analog signals for a week with less than 50-percent attenuation, although the fixed-pattern noise has increased relative to the uncycled value. Devices have been cycled more than 10^7 times but, pending further investigation, the conservative 10^6 figure seems advisable. For many applications, an endurance of only 10^3 cycles is ample.

Investigation of fixed-pattern noise reveals that it is caused by threshold-voltage variations in both the thin (~ 30 Å SiO_2) dielectric of the memory gates and the thick (700 Å SiO_2) dielectric of the transfer gates. The former variation is somewhat greater than the latter (factors of 2 or less) and is introduced by the tunneling process. The variations in memory threshold are truly fixed-pattern noise, however, in the sense that repeated writing under the same conditions produces the same variations. This is seen by comparing Figs. V-2(a) and (b). Figure V-2(c) is the output obtained under the same circumstances, but with the memory gate level raised and

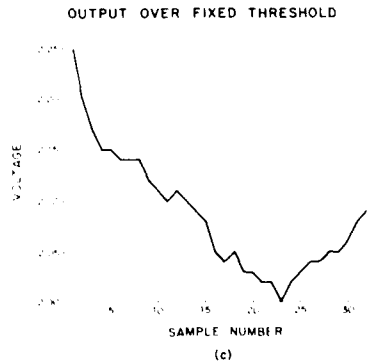
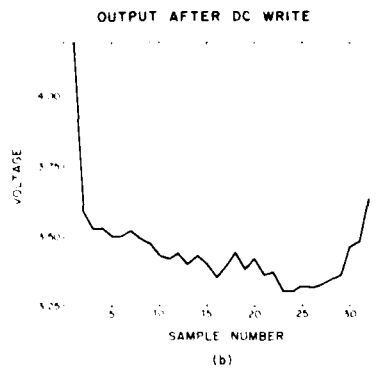
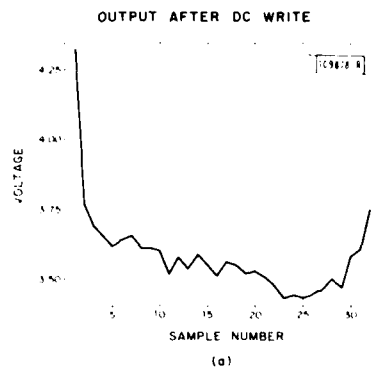


Fig.V-2. Fixed-pattern noise from the analog memory. (a) Output in normal operation after writing a uniform DC level into the memory. (b) Output after another write operation under the same conditions. Note the similarity to (a). (c) Output after a third write under the same write conditions, but with the read conditions modified to reflect the transfer-gate threshold instead of the memory-gate threshold.

the transfer gate level lowered during reading so that the latter's threshold determines the size of the output signal packets. Although the average slope of the noise in (b) and (c) is similar, there is no correlation of the sample-to-sample fluctuations and the rms deviation of the latter is somewhat less than that of the former.

Reset and source-follower MOSFETs connected to the parallel-holding-well electrode permit the operation of the device as a binary/analog memory correlator. The binary reference is stored in the memory sites, each of which either allows or blocks passage of the subsequently input analog signal to the parallel holding wells. The holding-well gate is used as a floating gate sensor to measure the sum of the transferred charge. The analog signal packets are then transferred back to the serial CCD channel, advanced one serial cell, and the correlation process is repeated.

Figure V-3 demonstrates the performance of this device in correlating a 15-bit M-sequence with itself. The first trace [Fig. V-3(a)] shows the output of the stored reference after three days of storage. The first two samples are unused sites which are kept closed (blocking parallel charge transfer). The remaining 30 sites contain the M-sequence, with the sequence 01 representing a (+) weight and the sequence 10 representing a (-) weight. The maximum amplitude (analog) input signal is seen at the top of Fig. V-3(b). This is a ± 1 -V-amplitude 15-bit repeating M-sequence with zero levels between bits. The output of the correlator is seen at the bottom of this photograph. Figure V-3(c) shows an input which has been attenuated by more than 40 dB and the corresponding output. Figure V-3(d) shows the input and output in the middle of this linear dynamic range. Figure V-3(e) was taken under the same conditions as (d) but with the input buried in a 10-kHz triangular wave. The suppression of this triangular interference is evident. These correlation waveforms were taken with a clock frequency of 12.5 kHz. With minor design changes, much higher frequencies could be reached.

In summary, the operating characteristics of the first-generation device (LTAM-A) are shown in Table V-1. The next generation analog memory has been designed and is now in the process of mask layout. Design characteristics of this device (LTAM-B) are shown in Table V-2.

R. S. Withers
R. W. Ralston

B. 2- TO 20-GHz-BANDWIDTH SUPERCONDUCTING MATCHED FILTER: DESIGN ANALYSIS

1. The Filter Concept

Microwave integrated circuit design, planar microfabrication technology, and superconducting metals are being combined in an effort to make very wideband analog signal-processing circuits. Filters matched to complex radar or communication signals such as linear-frequency-modulated (LFM) chirps or pseudonoise sequences appear feasible with time-bandwidth (TW) products of over 1000 and with bandwidths of 2 to 20 GHz. These filters will be synthesized using tapped delay lines with a waveguiding structure. Very long delay lines (1 to 50 n) having delays up to 0.50 μ s would fit on a small dielectric substrate (25 cm²). The waveguiding structure must be very narrow (5 to 100 μ m) to yield the long lengths. Resistive losses of normal metals in such narrow lines are prohibitive and thus a superconducting metal is required. Niobium (transition temperature $T_c = 9.2$ K) is preferred because it is very durable and has low loss at liquid-helium temperature (4.2 K). The technology for depositing and patterning it to

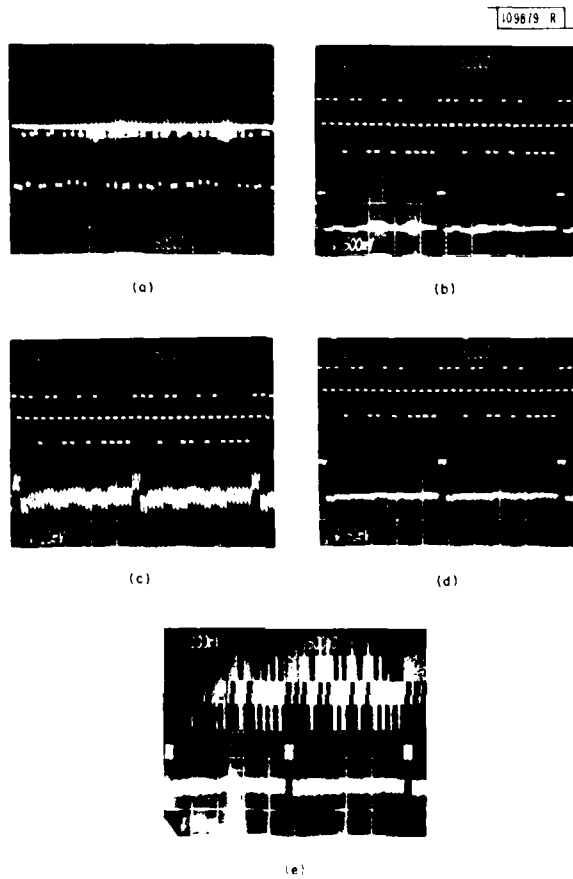


Fig.V-3. (a) Readout of the stored binary reference after 3 days of storage in the MNOS CCD. The 15-bit M-sequence is encoded differentially. 2 V/div. (b) Upper trace: input signal, a repeating M-sequence with zero levels between the bits. 4 V/div. Lower trace: correlation output, 500 mV/div. (c) Upper trace: input signal, 10 mV/div. Lower trace: correlation output, 10 mV/div. (d) Upper trace: input, 100 mV/div. Lower trace: correlation output, 50 mV/div. (e) Upper trace: same input as (d), with added interference signal. 100 mV/div. Lower trace: correlation output, 50 mV/div.

TABLE V-1 LTAM-A MNOS/CCD ANALOG MEMORY TYPICAL OPERATING PARAMETERS	
Reset Pulse Voltage	-35 V
Reset Pulse Length	10 ms
Write Pulse Voltage	+25 V
Write Pulse Length	200 μ s
CCD Clock Frequency	1 to 500 kHz
Charge Transfer Inefficiency	1.1×10^{-4} (14% fat zero, 125 kHz)
Endurance	$>10^6$ erase/write cycles
Dynamic Range	33 dB after 100 h

TABLE V-2 MNOS ANALOG MEMORY LTAM-B DESIGN AND OPERATIONAL FEATURES	
Memory	256 samples, $10 \times 10 \mu\text{m}^2$ memory area
CCD	3-phase, surface-n-channel, $10 \times 60 \mu\text{m}^2$ gate area
Technology	Dual-dielectric gate, one-level metal, two-level polysilicon interconnects Local oxidation of silicon channel stop, diffused source/drain
Chip Area	$8200 \times 800 \mu\text{m}^2$
Clock Speed	>1 MHz (input and output)
Voltage Gain	(serial input/store/serial output): approximately unity
Correlation	Binary/analog, 100-kHz rate

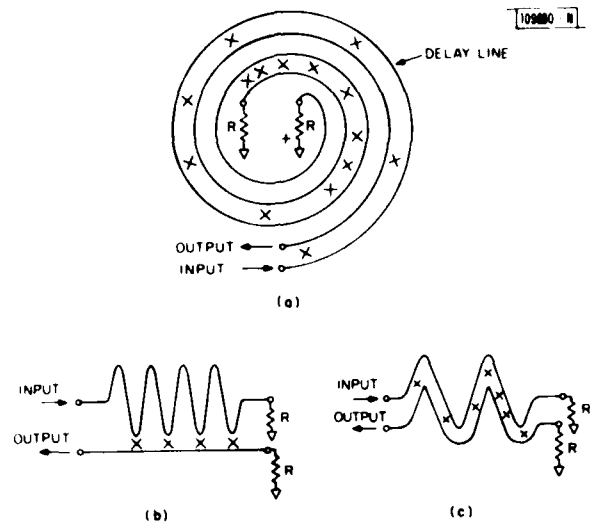


Fig. V-4. High-density delay-line patterns: (a) double spiral, (b) single meander, (c) double meander. The x marks tap positions.

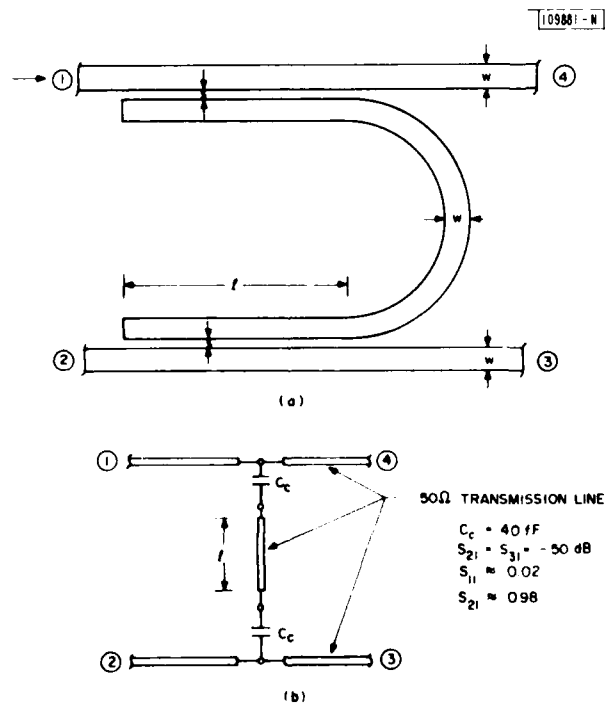


Fig. V-5. Wideband tap: (a) physical layout, (b) equivalent circuit.

1- μ m precision has been developed at Lincoln Laboratory and elsewhere. This report gives the results of an analysis of the theoretical and practical constraints on implementing such electromagnetic filters.

One penalty of using superconductors is that refrigerators are needed to maintain the cryogenic environment for the superconducting circuits. Such refrigerators are being developed. A spin-off from the superconducting computer development is a 4.2 K refrigerator which requires 2 kW of power. Under intensive development are refrigerators which operate at 10 to 12 K. These are designed for extended-mission spacecraft and require about 500 W of power. Superconductors with high T_c (e.g., Nb_3Sn , $T_c = 18$ K) are being developed and are well matched to the higher temperature refrigerators. Thus it is feasible to place superconducting circuits, both analog and digital, in future systems.

2. Analysis of Time-Bandwidth Constraints

The time-bandwidth constraints of the filter are determined by the delay line itself. The constraints imposed by conductor loss, dielectric loss, dispersion, crosstalk, and fabrication technologies are therefore examined for microstrip, stripline, and coplanar waveguide.

a. Tapped-Delay-Line Filter

Three different geometries for squeezing a very long tapped delay line on a small surface area are shown in Fig. V-4. The dual-spiral pattern is preferred for several reasons: tight radius bends are avoided and taps are placed independently of bends; the circular space is 100 percent utilized (thin wafer substrates are typically round); and spurious signals induced on the output line by crosstalk are propagating away from the output port, can be terminated, and are less likely to cause distortion.

A LFM filter can be synthesized with a tapped delay line in a variety of ways; two schemes are being studied. One approach is to divide the total frequency band into n channels. Each tap corresponds to one of the narrow bands and has an amplitude-vs-frequency characteristic designed to coherently add to the response of adjacent taps in order to give a unit amplitude response (or other desired weighting) across the band. In addition, a quadratic phase-vs-frequency characteristic must be achieved in order to give the desired linear group-delay-vs-frequency response. This requirement determines the placement of each tap in the delay line. Using this approach, a relatively small number of taps are required to synthesize large time-bandwidth-product filters. Each tap, however, is unique and is of complex design.

An alternate approach, which is much easier to fabricate but which introduces slight signal distortion, is to use wideband taps, all of which have positive weight and identical phase characteristics. The taps are placed nonuniformly along the delay line at delays corresponding to 360° of phase change in the chirp signal $S(t) = \cos(\omega_0 t + 1/2 \mu t^2)$, where μ is the chirp slope over the interval $-T/2 \leq t \leq T/2$. This approach was developed at Lincoln Laboratory³ for another project and gave good performance for a LFM signal with a TW product of 200. In general this technique is applicable for filters of TW product above about 100.

The physical layout and equivalent circuit of a wideband tap is shown in Fig. V-5. The weight of a typical tap would be set at -50 dB; thus multipath signals resulting from the nondirectionality of the tap would be very small relative to the desired signal.

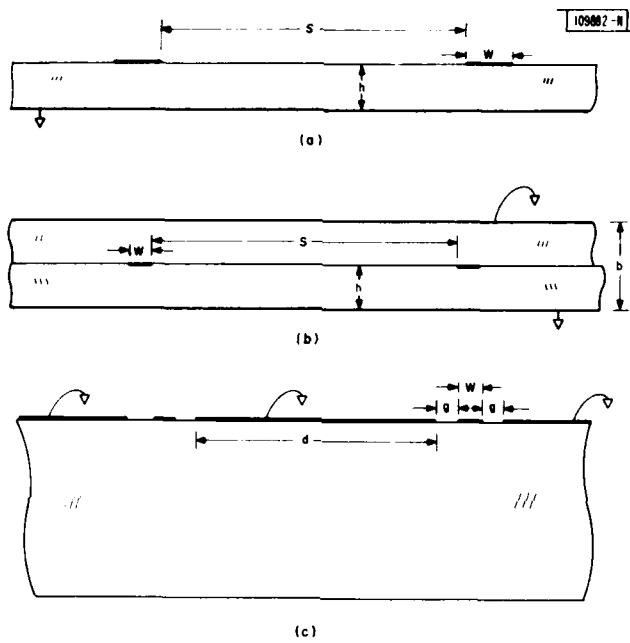


Fig. V-6. Waveguiding structures: (a) microstrip, (b) stripline, (c) coplanar waveguide.

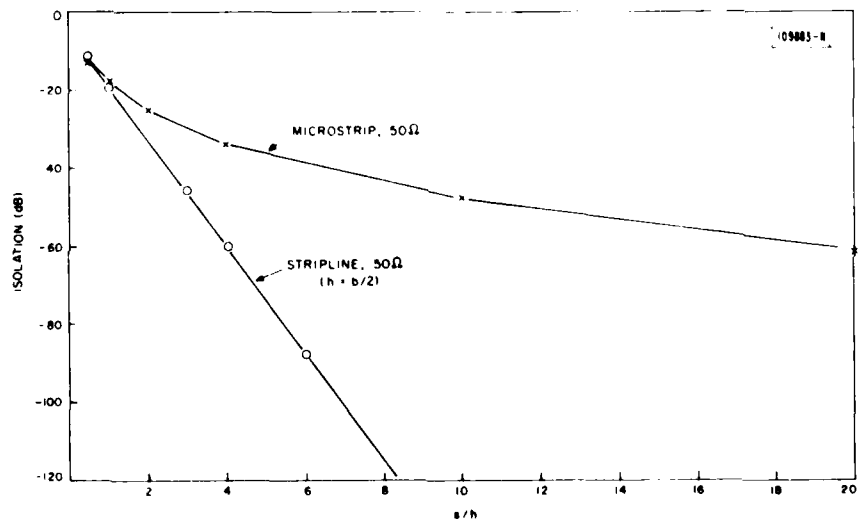


Fig. V-7. Coupling between parallel lines for stripline and microstrip.

b. Waveguiding Structures

The three waveguiding structures - microstrip, stripline, and coplanar waveguide - are shown in Fig. V-6. All three may be used under certain circumstances, and all are superior to such alternatives as slotline or slow-wave structures. The three structures have comparable losses (coplanar is about 2 dB greater). Stripline has no dispersion, but it will be seen that for the dimensions and frequencies important here all the structures have negligible dispersion. The three structures have very different crosstalk properties, and they stress fabrication technology quite differently. In the discussion that follows the filter is assumed to have 50 percent fractional bandwidth. A tapped-delay-line filter thus requires the line length L in wavelengths λ to equal $2TW$.

c. Crosstalk

Crosstalk between the input and output lines is significant as a loss mechanism for the spiral geometry, and as both a loss and distortion mechanism for other geometries. If the loss per wavelength is k_{ct} , then the delay-line loss in dB is $8.6 k_{ct} L/\lambda$. Thus $k_{ct} < 1/2TW$ gives an acceptable loss less than 8.6 dB.

The crosstalk is approximately given by $k_{ct} \approx (Z_{oo} - Z_{oe})/(Z_{oo} + Z_{oe})$ where Z_{oo} , Z_{oe} are the odd- and even-mode impedances of the input and output lines taken as a pair.

Figure V-7 shows the crosstalk coefficient for microstrip and stripline as a function of line spacing (for a 50Ω line). Microstrip has more crosstalk for wide spacing because of the absence of an upper ground plane. This can be somewhat alleviated by using shielded microstrip. The crosstalk for coplanar waveguide has not been analyzed. However, an analog simulation using conducting paper indicates that if $w = g$ and $d/g = 5$ (variables defined in Fig. V-6), the crosstalk is about -40 dB and if $d/g = 10$, it is -46 dB. The crosstalk for coplanar guide only drops inversely with the line spacing, while for stripline it drops exponentially. The reason for this is that the very thick dielectric of the coplanar guide allows for significant capacitance between the two lines, while in stripline the capacitance is very small because the ground plane intercepts nearly all field lines. Thus coplanar guide can be used on small time-bandwidth ($TW = 100$), microstrip on modest ($TW = 300$), and stripline on large ($TW = 2000$) delay lines. Practical stripline structures can be made where the crosstalk is virtually zero. The thrust of our first design and experimental efforts will be the microstrip and stripline geometries.

d. Conductor Loss

At microwave frequencies, superconductors have significant resistance due to the presence of normal electrons. The loss (in dB) for superconducting microstrip is $8.6 R_s L/wZ_o$, where L is the delay-line length, R_s the surface resistance of Nb, w the strip width, and Z_o the line impedance.

On an arbitrary large substrate one can design an arbitrary long delay line by making the conductor strip wide enough to ensure modest losses. On a fixed-area substrate, the delay-line length, the strip width, and the line impedance are interrelated. These relationships can be expressed as a function of the total delay and fractional bandwidth.

Consider a stripline of geometry shown in Fig. V-6. The physical length of the line $L = cT/\sqrt{k_p} = A/(s + w)$ where T is the total delay, $c/\sqrt{k_p}$ the propagation velocity in the line, and

A the substrate area. The loss (in dB) is $8.6 R_S L/wZ_0$. Evaluating this expression in terms of delay and bandwidth can be done with the following constraints appropriate to our filters:

$$s/b = 2 \text{ for } -60 \text{ dB crosstalk}$$

$$k_w = W/f_0 = \text{fractional bandwidth}$$

$$R_S = 5.5 \times 10^{-7} f^{1.7} \Omega/\square, \text{ f in GHz, for Nb at 4.2 K}$$

$$\text{Conductor loss (dB)} = \frac{5.2 \times 10^{-6} W^{1.7} T^2}{k_w^{1.7} Z_0 A k_r}$$

For $k_w = 1/2$, $k_r = 9.6$ (sapphire), $Z_0 = 50\Omega$ ($w/b = 0.167$), and $A = 25 \text{ cm}^2$, the loss (dB) = $2 \times 10^5 (TW)^2$.

This latter expression of the limits of filter design in terms of signal delay and bandwidth is shown in Fig. V-8. These constraints are not influenced very much by impedance level or dielectric constant. The constraints are very much influenced by operating temperature and the material T_c . Figure V-9 shows the dependence of maximum delay length for 10 dB loss at 2 GHz bandwidth vs temperature for Nb and Nb_3Sn .

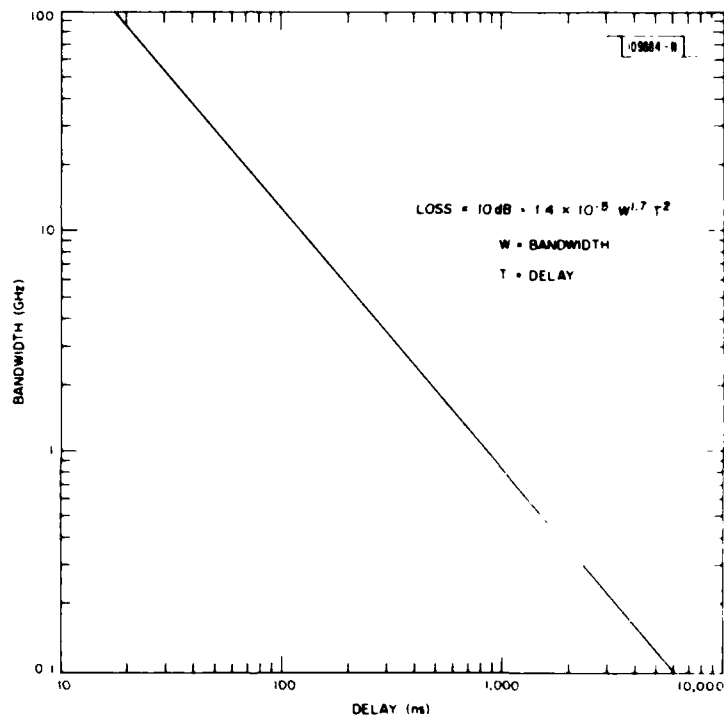


Fig. V-8. Delay-bandwidth constraint on superconducting stripline due to conductor loss.

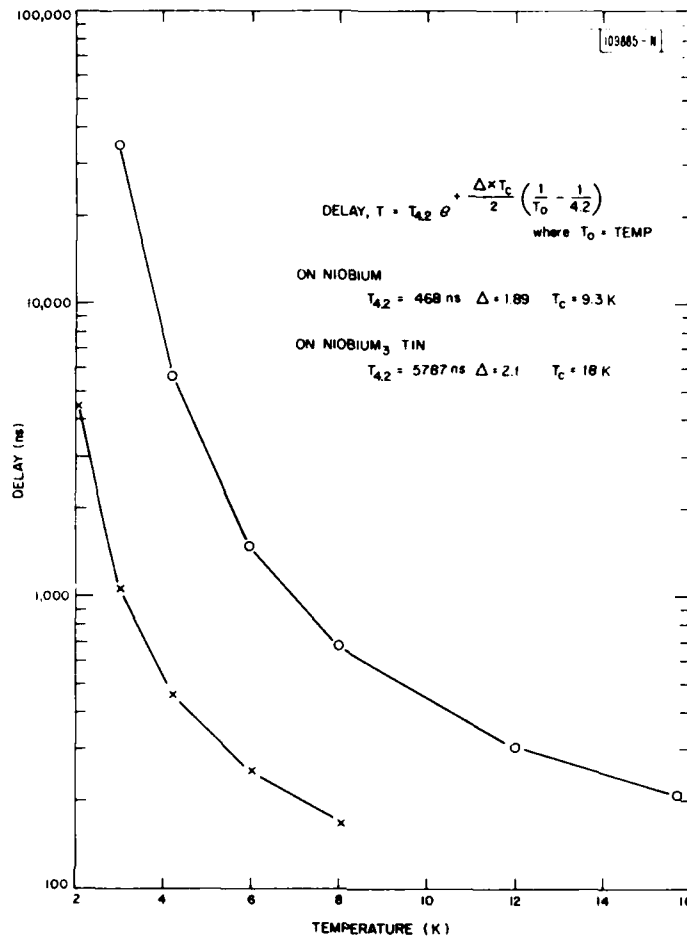


Fig. V-9. Maximum delay as a function of temperature for superconducting microstrip due to conductor loss.

From the curves we conclude that a chirp filter with $W = 2 \text{ GHz}$, $T = 0.5 \mu\text{s}$ is possible with Nb and that ultimately FW products of 10,000 are feasible with Nb_3Sn . It is also seen that a filter using Nb_3Sn can be operated at 10 to 12 K, the temperature range being addressed by the new refrigerator development.

c. Dielectric Loss and Dispersion

Superconducting microstrip, stripline, or coplanar waveguide will exhibit loss due to the dielectric. This loss (in dB) is approximately given by $8.6 \alpha_d L$, where $\alpha_d = (\pi \tan \delta) / \lambda$ and $\tan \delta$ is the loss tangent of the dielectric.

By evaluating this expression in terms of the delay and bandwidth of the delay line the loss is given by

$$\text{loss (dB)} = 8.6 \pi (\tan \delta) TW k_w$$

For 50 percent bandwidth ($k_w = 0.5$) and an acceptable loss of 5.4 dB, the constraint on the time-bandwidth product of the delay line is given by $TW < 1/(10 \tan \delta)$. Thus a $TW = 100$ filter requires a loss tangent of 10^{-3} , an easily met requirement. A $TW = 1000$ filter requires a loss tangent of 10^{-4} . Bulk Supercill II (a very pure quartz) has a loss tangent of about 10^{-4} . Sapphire has a loss tangent of 10^{-6} or better, making it the dielectric of choice.

The Getsinger model⁴ for microstrip dispersion is given by

$$\epsilon_e = \epsilon_s - \frac{\epsilon_s - \epsilon_{e0}}{1 + G f^2 / f_p^2}$$

where $f_p = Z_0 / 2 \mu_0 h$ is the cutoff frequency, ϵ_s is the substrate relative dielectric constant, ϵ_{e0} is the effective DC dielectric constant, $G \approx 1$, and Z_0 is the line impedance.

This dispersion places a limit on the TW product that a substrate of a given height can support. For the thin substrates of interest to this project this dispersion is negligible. For example, the cutoff frequency f_p is about 200 GHz for a 100- μm (4 mil) substrate, which results in a 0.01-percent change in the dielectric constant over a 2-GHz bandwidth.

Stripline is entirely free from dispersion, and thus even larger structures could be used if required. In general, however, dispersion is not a problem for any of the small waveguiding structures.

f. Fabrication Technology

The fabrication issues involve the dielectric substrate, the photolithography, and the niobium. Each is discussed below.

Coplanar waveguide places no constraint on the dielectric thickness. Stripline and microstrip require thin substrates to allow narrow lines near 50 Ω impedance (25 to 100 Ω is convenient). Table V-3 shows the maximum delay-line length of 50 Ω stripline for an array of substrate areas and thicknesses. Commercial vendors of precision microwave dielectric substrates can supply unsupported 2-in.-dia. low-loss sapphire substrates 100 μm thick; thus 50-ns delay is achievable in the near term. Thinner substrates ($\leq 25 \mu\text{m}$) may be feasible if supported by bonding to a thicker carrier. Such development will be required to reach delays of 200 ns or

TABLE V-3
DELAY-LINE LENGTH
50 Ω STRIPLINE ON SAPPHIRE

		Substrate Thickness (μm)			
		400	100	25.0	6.0
		Delay (ns)			
Active Area (cm^2)	5	3	12	50.0	200.0
	20	12	50	200.0	800.0
	40	24	100	400.0	1600.0
Line Width (μm)		133	33	8.3	2.1

greater. Alternate long-term development options for long delays on very thin substrates involve deposited dielectrics or sheet dielectrics. Fabrication of a thin-film dielectric with adequately low loss will require very low contamination in the deposited film. A more readily explored alternative would be to use plastic film as the dielectric. Films of Teflon, or polyethylene or polyimide are available in thickness of 1 mil (25 μm) or less. Loss tangents of 2×10^{-5} have been reported at 4.2 K. These films could be used to make microstrip by depositing and patterning Nb on the film directly or by sandwiching the film between two thicker substrates which carry the Nb ground plane and strip patterns.

Minimum feature sizes of 1 μm are readily achievable by contact photolithography over small areas. Because the waveguiding structures required line widths of 2 μm or greater, resolution itself is not a problem. However, the line should be free of defects over the large substrate surface. This places a limit on acceptable particulate contamination (e.g., the 200-ns line is 20 m long and can suffer no shorts, opens, or major perturbations in impedance). The reasonable limit determined by photolithography would be a delay of about 2 μs . Reaching this limit will require extensive development of a 3-in.-dia. photolithographic technology.

The low contamination required for the photolithography applies to the cleaning of the dielectric substrate and to the sputter process used for Nb deposition.

3. Summary

Current technology and the underlying physics support making delay lines of 50 ns delay and 2 GHz bandwidth. Thus a near-term goal of a 100 TW-product filter is realistic. Such a filter can be implemented with coplanar waveguide (without violating the crosstalk constraint), or stripline or microstrip (without violating the 4-mil substrate thickness fabrication constraint), or with a thin-film dielectric (without violating the dielectric-loss constraint).

All three alternatives are to be investigated experimentally. The eventual attainment of TW product delay lines with bandwidths of 5 to 20 GHz, will require major development effort. For stripline or microstrip, such development will require making thin (< 25 μm) substrates. For coplanar filters, it will require careful design to compensate for the crosstalk signal loss and distortion. Producing such wideband filters and other analog superconducting components promises large payoffs in signal processing systems.

J. T. Lynch

REFERENCES

1. Solid State Research Report, Lincoln Laboratory, M.I.T. (1979:2), pp. 70-74, DDC AD-A078676/4; Solid State Research Report, Lincoln Laboratory, M.I.T. (1980:3), pp. 49-53, DTIC AD-A094075.
2. Solid State Research Report, Lincoln Laboratory, M.I.T. (1981:1), pp. 53-54.
3. B. Loesch, E. M. Hofstetter, and J. P. Perry, "A Technique for Synthesizing Signals and Their Matched Filters," Technical Report 475, Lincoln Laboratory, M.I.T. (29 December 1969), DDC AD-704574.
4. W. J. Getsinger, IEEE Trans. Microwave Theory Tech. MTT-21, 34 (1973).

UNCLASSIFIED

SECURITY CLASSIFICATION OF THIS PAGE (When Data Entered)

REPORT DOCUMENTATION PAGE		READ INSTRUCTIONS BEFORE COMPLETING FORM															
1. REPORT NUMBER ESD-TR-81-95	2. GOVT ACCESSION NO. AD A110 947	3. RECIPIENT'S CATALOG NUMBER															
4. TITLE and Subtitle Solid State Research	5. TYPE OF REPORT & PERIOD COVERED Quarterly Technical Summary 1 February - 30 April 1981																
	6. PERFORMING ORG. REPORT NUMBER 1981:2																
7. AUTHOR Alan L. McWhorter	8. CONTRACT OR GRANT NUMBER F19628-S0-C-0002																
9. PERFORMING ORGANIZATION NAME AND ADDRESS Lincoln Laboratory, M.I.T., P.O. Box 73 Lexington, MA 02173	10. PROGRAM ELEMENT, PROJECT, TASK AREA & WORK UNIT NUMBERS Program Element No. 632501 Project No. 6491																
11. CONTROLLING OFFICE NAME AND ADDRESS Air Force Systems Command, USAF Andrew AFB Washington, DC 20331	12. REPORT DATE 15 May 1981																
	13. NUMBER OF PAGES 86																
14. MONITORING AGENCY NAME & ADDRESS (if different from performing org.) Electronic Systems Division Hanscom AFB Bedford, MA 01731	15. SECURITY CLASS (if different from report) Unclassified																
	15a. DECLASSIFICATION/DOWNGRADING SCHEDULE																
16. DISTRIBUTION STATEMENT (of this Report) Approved for public release; distribution unlimited.																	
17. DISTRIBUTION STATEMENT (of abstracts entered in Block 20, if different from Report)																	
18. SUPPLEMENTARY NOTES None																	
19. KEY WORDS (Continue on reverse side if necessary and identify by block number) <table border="0"> <tr> <td>solid state devices</td> <td>photodiode devices</td> <td>infrared imaging</td> </tr> <tr> <td>quantum electronics</td> <td>lasers</td> <td>surface-wave transducers</td> </tr> <tr> <td>materials research</td> <td>laser spectroscopy</td> <td>charge-coupled devices</td> </tr> <tr> <td>microelectronics</td> <td>imaging arrays</td> <td>acoustoelectric devices</td> </tr> <tr> <td>analog device technology</td> <td>signal processing</td> <td></td> </tr> </table>			solid state devices	photodiode devices	infrared imaging	quantum electronics	lasers	surface-wave transducers	materials research	laser spectroscopy	charge-coupled devices	microelectronics	imaging arrays	acoustoelectric devices	analog device technology	signal processing	
solid state devices	photodiode devices	infrared imaging															
quantum electronics	lasers	surface-wave transducers															
materials research	laser spectroscopy	charge-coupled devices															
microelectronics	imaging arrays	acoustoelectric devices															
analog device technology	signal processing																
20. ABSTRACT (Continue on reverse side if necessary and identify by block number) <p>This report covers in detail the solid state research work of the Solid State Division at Lincoln Laboratory for the period 1 February through 30 April 1981. The topics covered are Solid State Device Research, Quantum Electronics, Materials Research, Microelectronics, and Analog Device Technology. Funding is primarily provided by the Air Force, with additional support provided by the Army, DARPA, Navy, NASA, and DOE.</p>																	

DD FORM 1473 EDITION OF 1 NOV 65 IS OBSOLETE
1 JAN 73

UNCLASSIFIED

SECURITY CLASSIFICATION OF THIS PAGE (When Data Entered)

**DAT
FILM**